# The quantification of NOx and SO$_2$ point source emission flux errors of mobile DOAS on the basis of the Gaussian dispersion model: A simulation study

Yeyuan Huang[1,2], Ang Li[1], Thomas Wagner[4], Yang Wang[4], Zhaokun Hu[1], Pinhua Xie[1,2,3], Jin Xu[1], Hongmei Ren[1,2], Julia Remmers[4], Xiaoyi Fang[5], Bing Dang[6]

[1]Key Laboratory of Environmental Optics and Technology, Anhui Institute of Optics and Fine Mechanics, Hefei Institutes of Physical Science, Chinese Academy of Sciences, Hefei, 230031, China.

[2]University of Science and Technology of China, Hefei, 230026, China.

[3]CAS Center for Excellence in Regional Atmospheric Environment, Institute of Urban Environment, Chinese Academy of Sciences, Xiamen, 361000, China.

[4]Max Planck Institute for Chemistry, Mainz, Germany.

[5]Chinese Academy of Meteorological Science, Beijing, 100081, China.

[6]Beijing Municipal Climate Center, Beijing, 100089, China.

Correspondence to: Ang Li (angli@aiofm.ac.cn), Pinhua Xie (phxie@aiofm.ac.cn) and Yang Wang(y.wang@mpic.de)

**Abstract**: Mobile differential optical absorption spectroscopy (mobile DOAS) has become an important tool for the quantification of emission sources, including point sources (e.g., individual power plants) and area emitters (e.g., entire cities). In this study, we focused on the error budget of mobile DOAS measurements from point sources, and we also offered recommendations for the optimum settings of such measurements via a simulation with modified Gaussian plume model. Following the analysis, we conclude that: **(1)** The proper sampling resolution should be between 5 m and 50 m. **(2)** When measuring far from the source, undetectable flux (measured SCDs are under the detection limit) resulting by wind dispersion is the main error source. The threshold for the undetectable flux can be lowered by larger inte-

gration time. When measuring close to the source, low sampling frequency results in large errors and wind field uncertainty becomes the main error source of $SO_2$ flux (for NOx this error also increases, but other error sources dominate). More measurements times can lower the flux error that results from wind field uncertainty. The proper wind speed for mobile DOAS measurements is between 1 m/s and 4 m/s. **(3)** The remaining errors by [NOx]/[$NO_2$] ratio correction can be significant when measuring very close. To minimize the [NOx]/[$NO_2$] ratio correction error, we recommend minimum distances from the source, at which 5% of the $NO_2$ maximum reaction rate is reached and thus NOx steady-state can be assumed. **(4)** Our study suggests that emission rates $< 30$ g/s for NOx and $< 50$ g/s for $SO_2$ are not recommended for mobile DOAS measurements.

Based on the model simulations our study indicates that mobile DOAS measurements are a very well suited tool to quantify point source emissions. The results of our sensitivity studies are important to make optimum use of such measurements.

## 1 Introduction

Nitrogen oxides (NOx = NO + $NO_2$) and sulphur dioxide ($SO_2$), poisonous and harmful trace gases in the atmosphere, are critical participants in tropospheric chemical reactions (Seinfeld and Pandis, 1998; Beirle et al., 2003). NOx and $SO_2$ are emitted into the atmosphere via natural and anthropogenic emissions, especially from traffic and industries. In recent years, China has experienced large areas of haze pollution, which have drawn worldwide scrutiny due to their NOx, $SO_2$, and volatile organic compounds content, although strict policies designed to control the emission of pollution gases have been implemented (Richter, et al., 2005; Ding et al., 2015; Jin et al., 2016; Zhang et al., 2019, 2020). It is of great significance to study gas emission pollution both qualitatively and quantitatively.

Differential Optical Absorption Spectroscopy (DOAS) is a technique developed in the 1970s that focuses on the telemetering of atmospheric gases, particularly trace gases (Platt and Stutz, 2008). After years of research, various types of DOAS technology have been comprehensively developed, including LP-DOAS, MAX-DOAS, and mobile DOAS.

Mobile DOAS technology was originally used to measure volcanic $SO_2$ emissions (Bobrowski et al., 2003; Edmonds et al., 2003; Galle et al., 2003), and it was then developed to measure the $NO_2$ and $SO_2$ emission fluxes from industrial parks (Johansson et al., 2006). In 2008, Mattias Johansson used a mobile mini-DOAS device to quantify the total emission of air pollutants from Beijing and evaluated the measurement error, mainly in terms of the uncertainties in the wind field, experimental setup, sunlight scattering in the lower atmosphere, and DOAS fit error. During the MCMA 2006 field campaign, C. Rivera et al. (2009) used a mobile mini-DOAS instrument to measure the $NO_2$ and $SO_2$ emissions of the Tula industrial complex in Mexico and also estimated the flux error. In O. Ibrahim et al. (2010), T. Wagner et al. (2010), and R. Shaiganfar et al. (2011, 2017), air mass factor (AMF), sampling resolution, NOx chemical reactions, and atmospheric lifetime were introduced in order to analyze the emission flux error. The analysis of emission flux error sources has gradually come to focus on the wind field uncertainty, sampling resolution measurement error (GPS error), Slant Column Density (SCD) fit error, AMF error, and other error sources. The aforementioned studies primarily concentrated on regional/industry park emission fluxes, as opposed to point sources.

Different from regional/industry park measuring, point source emission flux can be measured in diverse ways, with different measuring distances, varying sampling resolutions, and so on. Therefore, the error sources and influence factors affecting the flux measurements are different. In order to investigate the impact of these factors and thereby recommend optimum settings for point source flux measuring using mobile DOAS, we performed an in-depth study on the effects of error sources and influence factors on point source emission flux measuring.

There are innate deficiencies in the experimental method used to analyze the emission flux error since there are so many scenarios that need to be verified, and the various factors cannot be well controlled during experiments. Therefore, a convenient way to assist the analysis is sorely needed. In the absence of precise requirements, the simulation method is a good alternative for facilitating the analysis of mobile DOAS emission flux error, given its convenience and feasibility.

84    Using a model based on Gaussian plume dispersion and the mobile DOAS emission flux

85    measurement method, we here performed a simulation to study the measurement of NOx and

86    SO$_2$ point source emission flux.

87    This paper is organized as follows: In Section 2, the methodological framework is present-

88    ed. In Section 3, the parameters used to drive the simulation are delineated. Section 4 de-

89    scribes the simulation performance and data analysis, Section 5 presents our conclusions, and

90    the Appendix displays the overall simulation results.

91    **2 Methodology and forward model**

92    **2.1 Overview of methodology**

93    The NOx and SO$_2$ emission flux of the point source can be well measured by the mobile

94    DOAS. The equation for calculating the emission flux in the discrete form is expressed as

$$F = \sum_j VCD_j \cdot \vec{u_j} \cdot \vec{n_j} \cdot s_j \qquad (1)$$

96    where $F$ is the emission flux; $VCD_j = SCD_j / AMF_j$, $SCD_j$ is the SCD for mobile DOAS

97    measurements along the measurement route; $AMF_j$ is the Air Mass Factor; $\vec{u_j}$ is the wind

98    field; $\vec{n_j}$ is the vector pointing to the right of the driving direction and parallel to the Earth's

99    surface; and $s_j$ is the sampling resolution. For an isolated point source, the mobile DOAS

100   can measure underneath the plume in downwind direction to quantify the emission flux.

101   Since individual experiments take place in complex and variable scenarios, in order to in-

102   vestigate the error sources and influence factors that impact the flux measurement error, typi-

103   cal mobile DOAS measurements of the NOx and SO$_2$ emission fluxes were modeled with the

104   following assumptions:

105   (1) NOx and SO$_2$ gas continuously exhaust from an isolated and elevated point source at

106   the position (0 m, 0 m, 235 m). The plume rises approximately 15 m.

107   (2) The plume is diluted by the wind along the wind direction ($x$ axis). The random move-

108   ment of air parcels dilute the plume also in the cross-section and in the vertical directions ($y$

109   axis and $z$ axis).

110   (3) The topography around the point source is flat and the background concentration of the

111     pollutants is regarded as zero. In case of non-negligible background concentrations, the VCDs

112     in the plume have to be calculated as difference to the background.

113     (4) Air turbulence is constant in space and time.

114     (5) A zenith-sky mobile DOAS measures the gas underneath the plume in the *y*-direction at

115     around noon (see Figure 1). Spectra, GPS data, and wind profiles are available for individual

116     measurements.

117     (6) The sunlight radiance received by the mobile DOAS instrument is stable.

118     Figure 1 presents the schematic diagram of the modeled mobile DOAS measurement of a

119     point source.
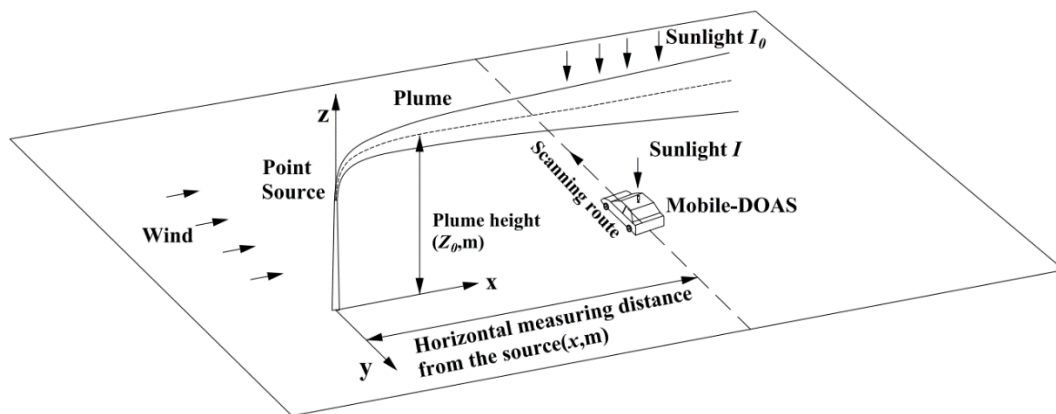
120

121     Figure 1. Schematic diagram of the modeled mobile DOAS measurement underneath the plume.

122     Based on the performance of typical mobile DOAS measurements, a forward model of flux

123     calculations was generated and error analysis performed according to the forward model, as

124     shown in Figure 2.

125
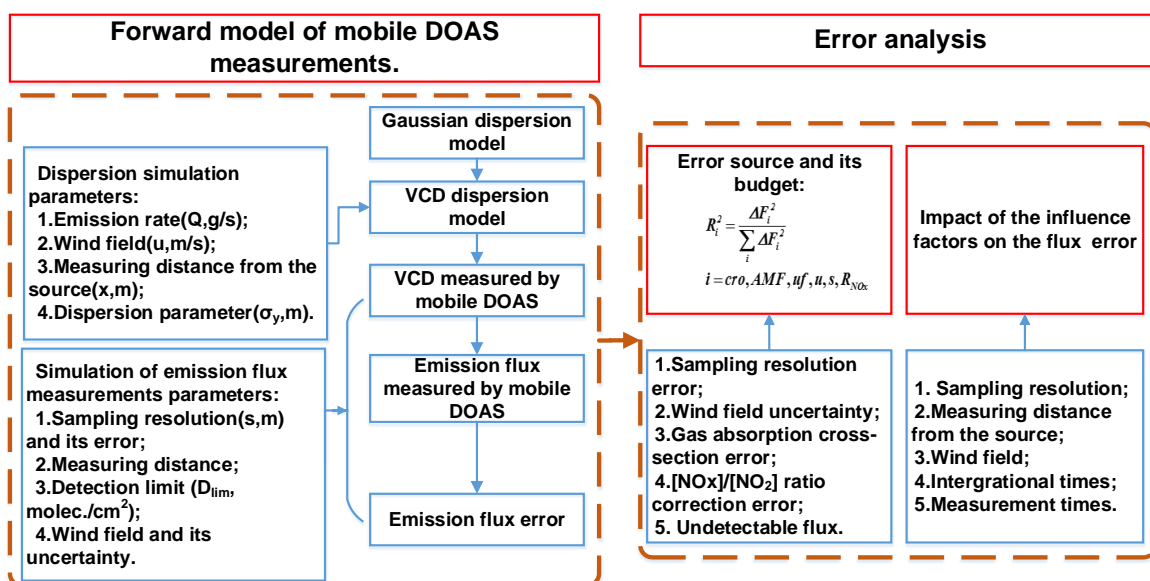
Figure 2. Forward model of mobile DOAS measurements and error analysis.

The forward model of mobile DOAS measurements can be divided into 2 steps:

(**1**) Dispersion simulation. In this step, a dispersion model is established to generate the vertical column densities (VCDs) measured by the mobile DOAS in the modeled typical measurement.

(**2**) Simulation of emission flux measurement. After the VCD sequence along the measurement route is generated, the next step is calculating the emission flux and the emission flux error.

Error analysis:

This step concentrates on the error sources and their budget, and the influence factors that affect the emission flux error.

The emission flux and VCD retrieval calculation model can be directly introduced into our forward model, as it has in previous studies. However, some questions concerning the forward model still exist:

(**1**) Is the existing dispersion model suitable for the mobile DOAS measurement depicted in Figure 1?

(**2**) How can VCDs be simulated in the same way as mobile DOAS measurements in theory?

(**3**) Mobile DOAS can measure $NO_2$ instead of NOx. How can the $NO \leftrightarrow NO_2$ conversion be added to the existing dispersion model in terms of this simulation?

These questions will be explored in Sections 2.2–2.6.

**2.2 Description of Gaussian dispersion model**

**2.2.1 Steady-state Gaussian dispersion model**

An appropriate air dispersion model needed to be chosen for generating the forward model of mobile DOAS measurements. Since the concentrations of pollutants at individual points in in the air parcels of the plume under the assumptions we have made can be calculated based on the Gaussian dispersion model (Arystanbekova et al., 2004; Lushi et al., 2010; de Visscher, 2014), we applied the Gaussian dispersion model in this study. The plume, as reflected by the surface due to the ground boundary effect and the dispersion model, can be expressed as Eq.

155    (2).

156
$$c(x,y,z) = \frac{DQ}{2\pi u\sigma_y\sigma_z}\exp(-\frac{y^2}{2\sigma_y^2})\cdot\{\exp[-\frac{(z+H)^2}{2\sigma_z^2}]+\exp[-\frac{(z-H)^2}{2\sigma_z^2}]\}$$    (2)

157    where Q is the emission rate (g/s); u is the wind speed (m/s) and the wind direction is along

158    the $x$-direction; $\sigma_y$ (m) is the dispersion parameter in the $y$-direction; $\sigma_z$ (m) is the dispersion

159    parameter in the $z$-direction, with $\sigma_y$ and $\sigma_z$ dependent on $x$; and H is the plume height

160    (m). $D = \exp(-\varphi\frac{x}{u})$ is the decay term, mainly consisting of the chemical reactions and de-

161    posits; $\varphi$ is the decay coefficient; and $\varphi = \frac{\ln 2}{T_{1/2}}$, in which $T_{1/2}$ is the pollutant half-life in

162    seconds.

163        The dispersion parameters are determined by the atmospheric stability. The classification of

164    atmospheric stability, which was created by Pasquill and Gifford and is widely used, sorts at-

165    mospheric stability into 6 classes ranging from A–F (de Visscher, 2014). We only considered

166    the classifications under strong solar radiation (see Table 1) in this study.

167                        Table 1. Pasquill–Gifford atmospheric stability classifications.

| Wind Speed at 10m above the surface (m/s) | Strong Solar Radiation class |
|---|---|
| < 2 | A |
| 2~3 | between A and B |
| 3~5 | B |
| 5~6 | C |
| >6 | C |

168        A: very unstable; B: moderately unstable; C: slightly unstable

169        Based on the atmospheric stability class and the terrain type surrounding the emission point,

170    the parameters $\sigma_y$ and $\sigma_z$ can be calculated. Since we assumed the surrounding area to be

171    flat, rural terrain, the $\sigma_y$ and $\sigma_z$ parameters could be calculated using Briggs's (1973)

172    formulas, listed in Table 2.

173                        Table 2. Rural area air dispersion parameters (Briggs, 1973).

| Stable classes | $\sigma_y(x)$ | $\sigma_z(x)$ |
|---|---|---|
| A | $0.22x(1+0.0001x)^{-0.5}$ | $0.2x$ |

| | | |
|---|---|---|
| B | $0.16x(1+0.0001x)^{-0.5}$ | $0.12x$ |
| C | $0.11x(1+0.0001x)^{-0.5}$ | $0.08x(1+0.0002x)^{-0.5}$ |

174    in which $x$ is the horizontal distance from the source, m.

175    It should be noted that Briggs's equations are only suitable under the condition of $x$ lower

176    than 10 km. The dispersion in the wind direction is negligible in comparison with the advec-

177    tion when the wind speed is high, or for weak turbulence (de Visscher, 2014). In addition, the

178    model accuracy significantly decreases in the case of wind speeds < 1 m/s. The critical wind

179    speed for the Gaussian dispersion model is about 1.2m/s (de Visscher, 2014). For high wind

180    speed, the effect of undetectable flux becomes very important (see e.g. results in Fig. 8). Thus

181    for the general cases considered here measurements under high wind speed are not recom-

182    mended. Only for very high emissions and close to the source (< 1km), measurements for

183    high wind speeds might be meaningful, but such situations might be rare. Since our study fo-

184    cuses on the general cases, we limit it to wind speeds < 8m/s, because in the range up to 8m/s

185    the general dependencies become obvious. Therefore, the wind speed range in our simulation

186    is between 1.2 m/s and 8 m/s. The distance in our simulation is within 10km.

187    **2.2.2 NOx dispersion**

188    Eq. (2) is suitable for $SO_2$ dispersion, while for NOx, mobile DOAS can only measure $NO_2$

189    effectively. Hence, Eq. (2) should be adjusted for $NO_2$ dispersion based on NOx atmospheric

190    chemical reactions. In this study, we did not take Volatile Organic Compounds (VOCs) into

191    consideration; thus, a NOx balance would not be broken. Moreover, we assume that no NOx

192    is presented in the ambient air and no $O_3$ is consumed in the reaction with NO. In most cases,

193    both assumptions are reasonable, especially as long as the background NOx concentration has

194    no strong spatial-temporal variation. However, for very high emission rates, the assumption

195    that no $O_3$ is consumed in the reaction with NO might be violated (a simple criterion to iden-

196    tify such cases might be to check whether the NOx mixing ratios are higher than the ambient

197    $O_3$ mixing ratios). If this is the case, the conversion of NO to $NO_2$ will be delayed. The typical

198    reactions of NO, $NO_2$, $O_3$, and $O_2$ in the air parcels of the plume are:

199 $$NO_2 + h\nu \rightarrow NO + O(^3P) \qquad\qquad (\text{reaction } 1)$$

200 $$O_2 + O(^3P) \rightarrow O_3 \qquad\qquad (\text{reaction } 2)$$

201 $$NO + O_3 \rightarrow NO_2 + O_2 \qquad\qquad (\text{reaction } 3)$$
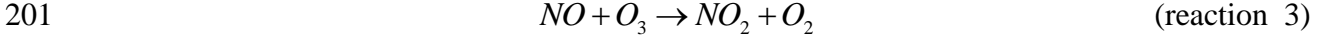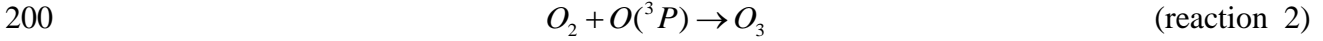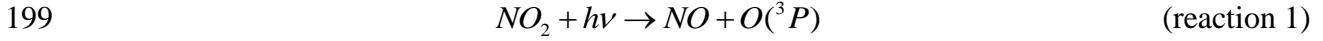
202     The reaction rates of reactions 1, 2 and 3 form a cyclic reaction. The reaction rate of $NO_2$

203 is:

204 $$r_{NO2} = -j_3[NO_2] + k_5[NO][O_3]_t \qquad\qquad (3)$$

205 where [gas] stands for the concentration of a particular gas; $[O_3]_t$ is the $O_3$ concentration in

206 the air parcels of the plume at time $t$; $t$ is the time period after NOx is emitted into the atmos-

207 phere. We assumed that at the beginning there is no $O_3$ in the air parcels of the plume. During

208 the mixing with outside air, the $O_3$ concentration within the air parcels increases. For simplic-

209 ity, we assumed that the $O_3$ concentration is the same everywhere in a transect of the plume. $j_3$

210 is the $NO_2$ photochemical rate constant, equal to approximately $8 \times 10^{-3} \, \text{s}^{-1}$; and $k_5$ is the rate

211 constant of reaction 3, equal to approximately $1.8 \times 10^{-14}$ $\text{cm}^3 \text{molecules}^{-1} \text{s}^{-1}$ (de Visscher,

212 2014). It should be noted that these rates are for a temperature of 25 ℃. Fortunately, they are

213 not sensitive to temperature, so temperature sensitivity did not need to be considered.

214     The [NOx]/[$NO_2$] ratio depends on the mixing ratio of $O_3$ inside the plume. The mixing ra-

215 tio of $O_3$ within the air parcel of the plume can then be estimated as:

216 $$[O_3]_t = [O_3]\frac{V_t - V_0}{V_t} = [O_3]\frac{S_t \Delta t - S_0 \Delta t}{S_t \Delta t} = [O_3](1 - \frac{S_0}{S_t}) \qquad\qquad (4)$$

217 where $V_0$ is the initial gas volume of the plume and $S_0$ is the initial gas cross-section of the

218 plume; while $V_t$ is the gas volume of the plume at time $t$ and $S_t$ is the gas cross-section of

219 the plume in the atmosphere at time $t$. Here, $[O_3]$ is the ambient $O_3$ concentration. The $NO_2$

220 concentration inside the plume at time $t$ is given by:

221 $$[NO_2]_t = \int_0^t r_{NO2} dt \qquad\qquad (5)$$

222     Since the $NO_2$ initial concentration was very low, we assumed the $NO_2$ initial concentration

223     $[NO_2]_0 = 0$. Consequently, $[NOx]_t = [NO]_0$ (with no decay).

224     The [NOx]/[NO$_2$] ratio at time $t$ is:

225

$$R_{NOx} = \frac{[NOx]_t}{[NO_2]_t} \tag{6}$$

226     Different from SO$_2$, the number of NOx molecules is conserved, as opposed to their mass.

227     The NOx dispersion model should thus be expressed as:

228

$$c_{NOx}(x,y,z) = \frac{DQ_{mNOx}}{2\pi u \sigma_y \sigma_z} \exp(-\frac{y^2}{2\sigma_y^2}) \cdot \{\exp[-\frac{(z+H)^2}{2\sigma_z^2}] + \exp[-\frac{(z-H)^2}{2\sigma_z^2}]\} \tag{7}$$

229     where $Q_{mNOx} = \frac{Q \cdot NA}{m_{NOx}}$. $m_{NOx}$ is the mean molar mass of the initial NOx and NA is Avoga-

230     dro's constant of $6.02 \times 10^{23}$ molecules mol$^{-1}$. Substituting Eq. (6) into Eq. (7), the NO$_2$ dis-

231     persion model can then be expressed as:

232

$$c_{NO2}(x,y,z) = \frac{c_{NOx}(x,y,z)}{R_{NOx}} \tag{8}$$

233     **2.3 VCD dispersion model**

234     As discussed above, mobile DOAS retrieves the VCD, while results of the dispersion mod-

235     el are point concentrations of the air parcels. Based on the definition of VCD, we integrate the

236     concentration along the vertical direction, i.e., the $z$-direction from the ground to the upper

237     troposphere, as in:

238

$$VCD(x,y) = \int_0^{+\infty} Dc(x,y,z)dz = \frac{DQ}{\sqrt{2\pi}u\sigma_y\sigma_z} \int_0^{+\infty} \{\exp[-\frac{(z+H)^2}{2\sigma_z^2}] + \exp[-\frac{(z-H)^2}{2\sigma_z^2}]\}dz$$

$$= \frac{DQ}{\sqrt{2\pi}u\sigma_y} \exp(-\frac{y^2}{2\sigma_y^2}) \tag{9}$$

239     Eq. (9) is suitable for SO$_2$. For NOx, the VCD dispersion is

240

$$VCD_{NOx}(x,y) = \frac{DQ_{mNOx}}{\sqrt{2\pi}u\sigma_y} \exp(-\frac{y^2}{2\sigma_y^2}) \tag{10}$$

241     The NO$_2$ VCD dispersion model is

242

$$VCD_{NO2}(x,y) = \frac{VCD_{NOx}(x,y)}{R_{NOx}} \tag{11}$$

243     Since NOx disperses along the wind direction and $R_{NOx}$ is a function of $t$, this means that

244     $R_{NOx}$ also varies with distance. The detailed relationship between the distance and $R_{NOx}$ will

245  be discussed in subsection 4.4. Eqs. (9), (10), and (11) lay the mathematical foundation of the

246  VCD distribution model for mobile DOAS measuring.

247  **2.4 VCD measured by mobile DOAS**

248  As shown in Figure 3, the flux of the plume cross-section can be calculated using the fol-

249  lowing equation:

250
$$\Delta F_j = u \cdot \int_l VCD(x, y)ds \tag{12}$$

251  $\Delta F_j$ is the flux along the measurement route $l$ in theory. For mobile DOAS measurement,

252  $\Delta F_j$ should be given by Eq. (13)

253
$$\Delta F_j = VCD_j \cdot u \cdot s_j \tag{13}$$

254  where $s_j$ is the distance between 2 measuring points and $VCD_j$ can be derived from the spec-

255  trum of measurement $j$. Based on Eqs. (12) and (13), $VCD_j$ can be expressed by Eq. (14)

256
$$VCD_j = \frac{1}{s} \int_l VCD(x, y)ds \tag{14}$$

257  Eq. (14) indicates that the $VCD_j$ derived from individual mobile DOAS measurements is the

258  average of $VCD(x,y)$ along the measurement route. The discretization of the VCD can signifi-

259  cantly affect the emission flux error and will be discussed in Section 4.1.
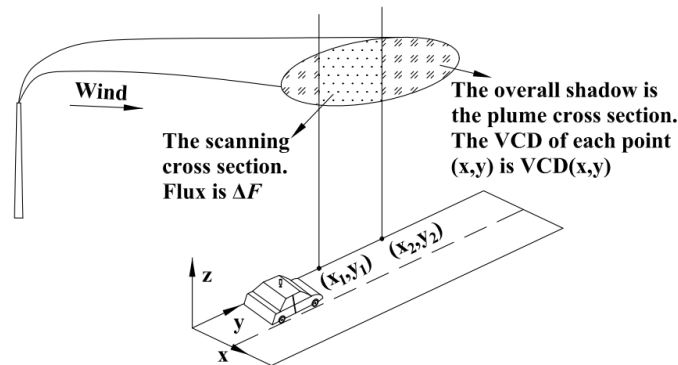
260
261  Figure 3. Model of VCD measured by mobile DOAS

262  **2.5 Description of emission flux measured by mobile DOAS**

263  Since the $SO_2$ lifetime scale is longer than the dispersion time scale, a decay correction is

264  not needed for $SO_2$, but for NOx it can be necessary. The $SO_2$ emission flux is then using Eq.

265  1 to calculate, while the NOx emission flux is:

$$266 \qquad\qquad\qquad F_{NOx} = \frac{R_{NOx}}{D} F_{NO2} \qquad\qquad\qquad (15)$$

267      In fact, the decay correction for NOx should be applied for cases with low wind speeds,

268      while the effect for high wind speeds is very small.

269      **2.6 Measurement errors of emission flux**

270      Emission flux measurements errors not only arise from measurement errors but also depend

271      on other factors, such as wind speed, measuring distance, [NOx]/[NO$_2$] ratio and the sampling

272      resolution.

273      Since the VCD is inversely proportional to the wind speed (Eqs.9 and 10), the higher the

274      wind speed is, the lower the VCD. This means more measurements at the edge of plume

275      would be under the detection limit at higher wind speeds causing more undetectable flux. The

276      VCD is also inversely proportional to measuring distance (Eqs.9 and 10). This means that the

277      undetectable flux increase with measuring distance. Since the [NOx]/[NO$_2$] ratio depends on

278      the measuring distance (see figure 10), a large [NOx]/[NO$_2$] ratio correction error occurs

279      when the measuring distance is small. Finally, the sampling error can be reduced with im-

280      proved sampling resolution.

281      The emission flux measurement errors by mobile DOAS have several sources: SCD fit er-

282      rors, AMF errors, wind field uncertainties, and sampling resolution measurement errors (Jo-

283      hansson et al., 2008, 2009; Wagner et al., 2010; Ibrahim et al., 2010; Shaiganfar et al., 2011,

284      2017; Rivera, et al., 2012).

285      The uncertainty of the derived SCD from the DOAS fit has a random and systematic part.

286      For the random part it can be assumed that in general it cancels out (in combination with the

287      sampling resolution error it can have a very small contribution). Thus, its direct effect on the

288      total flux error is neglected in the following. However, from the fit error also the detection

289      limit is estimated. For SCDs below the mobile DOAS detection limit, undetectable SCDs re-

290      sult in undetectable flux and therefore the fit error indirectly contributes to the total flux error.

291      The systematic part of the SCD error caused by the uncertainty of the trace gas absorption

292      cross-section is independent from the SCD fit error and is therefore included as an additional

293      term in the total flux error calculation.

294    We assume that these errors are random, have a Gaussian distribution and are independent

295    of each other. Then the total relative error of the emission flux is given by:

296
$$E_{total} = \frac{F_{err}}{D \cdot Q} \times 100\% = \frac{\sqrt{\Delta F_{cro}^2 + \Delta F_{uf}^2 + \Delta F_{AMF}^2 + \Delta F_u^2 + \Delta F_s^2}}{D \cdot Q} \times 100\%$$
(16)

297    where $F_{err}$ is the total flux error; $\Delta F_{cro}$ is the flux error introduced by gas absorption

298    cross-section error; $\Delta F_{uf}$ is the undetectable flux; $\Delta F_{AMF}$ is the flux error introduced by

299    AMF errors; $\Delta F_u$ is the flux error introduced by wind speed uncertainty. The wind direction

300    uncertainties play a smaller role in point source flux measuring error (and can be derived from

301    geometry), thus the uncertainties caused by the wind field are dominated by the wind speed

302    uncertainties. The error term of the wind direction uncertainty is therefore removed. $\Delta F_s$ is

303    the emission flux error introduced by sampling resolution measurement error and it can be

304    neglected (see section 4.1).

305    Eq. (16) is appropriate for SO$_2$. With regard to NOx, the NOx flux error is also introduced

306    by the decay correction and the [NOx]/[NO$_2$] ratio correction error. Hence, the NOx flux rela-

307    tive error is:

308
$$E_{NOx} = \frac{F_{err}}{D \cdot Q} \times 100\% = \frac{\sqrt{\Delta F_{R_{NOx}}^2 + \Delta F_{cro}^2 + \Delta F_{uf}^2 + \Delta F_{AMF}^2 + \Delta F_u^2 + \Delta F_s^2}}{D \cdot Q} \times 100\%$$
(17)

309    where $\Delta F_D$ is the flux error due to decay correction, and $\Delta F_{RNOx}$ is the flux error due to

310    [NOx]/[NO$_2$] ratio correction.

311    In order to quantify the contributions/budget of individual error sources, the ratios are cal-

312    culated as Eq. (18)

313
$$R_i^2 = \frac{\Delta F_i^2}{F_{err}^2}$$
(18)

314    where $i$ represents the individual error sources. Note that $\sum_i R_i^2 = 1$.

315    **3 Parameter assumption and numerical simulation**

316    In Section 2, the forward model for mobile DOAS measurements of emission flux was es-

317    tablished. In this section, reasonable values of the parameters in the forward model are dis-

318    cussed and prepared in order to drive the forward model.

319         For most factories, including power plants, the emission rates of NOx and $SO_2$ are different.

320    Since a higher emission rate is an ideal condition for mobile DOAS measurements, higher

321    emissions could be outside the scope of our study. Therefore, the emission rate that we simu-

322    lated was < 200 g/s, and we set the Q value within this range. Since the Gaussian dispersion

323    model is appropriate for moderate wind speed and scale, the wind speed was set to range from

324    1.2~8 m/s and the dispersion distance was approximately 0~10 km. Given the car speed and

325    mobile DOAS spectrometer integration times $t_{int}$ , the sampling resolution was set from 5–

326    500 m. The NOx mean daytime lifetime is approximately 5 h $\pm$ 1 h (Spicer, 1982), while

327    the $SO_2$ daytime lifetime is more than 1 day (S. Beirle, 2014). Compared with the dispersion

328    time scale, the $SO_2$ daytime lifetime uncertainty could be neglected. When time approaches

329    infinity, the NOx reaction steady-state could be determined by ambient $[O_3]$ according to Eq.

330    (5). We here assumed a typical $[O_3]$ value $1.389\times10^{12}$ molecules $cm^{-3}$ thus the steady-state

331    $[NOx]/[NO_2]$ ratio is 1.32. The $[NOx]/[NO_2]$ ratio inside the air parcel of the plume varying

332    with the distance could be determined by Eqs. (5), (6), (7) and (8).

333         The SCD error can mainly be attributed to the DOAS fitting error of the SCD and the trace

334    gas absorption cross-section error. Previous studies have indicated that the typical fit errors of

335    $NO_2$ and $SO_2$ SCDs are $\pm(1$~$4)$ $\times10^{15}$ molecules $cm^{-2}$ and $\pm(1$~$6)$ $\times10^{15}$ molecules $cm^{-2}$,

336    respectively (Wagner et al., 2011; Wang et al., 2014; Wu et al., 2018; Davis et al., 2019). Thus

337    in this study, we set the fit error of $NO_2$ and $SO_2$ to be $\pm2.5\times10^{15}$ molecules $cm^{-2}$ and $\pm$

338    $4\times10^{15}$ molecules $cm^{-2}$ (1σ error), respectively. Here in addition, we use the 2σ values as de-

339    tection limit (see e.g. Alicke et al., 2002; Platt and Stutz, 2008). The absorption cross-section

340    errors are less than 3% for $NO_2$ and less than 2.4% for $SO_2$ (Vandaele et al., 1994, 1998). In

341    this study, we set the total SCD error from gas absorption cross-section errors to 5% (Theys,

342    et al., 2007) for both $NO_2$ and $SO_2$. Of course, these values are only rough estimates, but they

343    are useful to investigate the general dependencies of the total flux error.

344         VCDs are derived from SCDs applying AMF. We calculated AMFs using the Monte Carlo

345 atmospheric radiative transfer model McArtim (Deutschmann et al., 2011). For that purpose,

346 we calculated 3-D box-AMF for different aerosol loads and solar zenith angle (SZA). It

347 should be noted that the application of 3-D box-AMF (in contrast to 1-D box-AMF) is im-

348 portant for the measurements considered in our study, because horizontal extension of the

349 plumes perpendicular to the wind direction is rather short (compared to the average horizontal

350 photon path lengths). Our simulations indicate that, for a plume height around 250m, the

351 AMF is typically between 1.05 and 1.3. The higher values are for high aerosol load and high

352 SZA (here only measurements below 75 °are considered), the lower values are for low aerosol

353 load and low SZA. In this study, we use an AMF of 1.15 and assume an AMF error of $\pm 10\%$.

354 For layer heights below 50m, the AMF is around 1.03 and the AMF error can be neglected.

355 The sampling resolution measurement error is primarily attributed to the drift of GPS.

356 However, flux error due to GPS drift could be neglected (see subsection 4.1).

357 The flux error due to wind field uncertainty mainly comes from wind speed uncertainty. In

358 order to quantify the wind speed uncertainties, the 1-month wind profile data at the height of

359 250 m during the time period 9:00~16:00 from 1 April–30 April 2019 were derived from the

360 Doppler wind profile radar located in Shijiazhuang (38.17 °N, 114.36 °E). The average wind

361 fields and standard deviations were calculated for each hour, as shown in Figure 4. Two-order

362 polynomials were applied in order to derive the function of standard deviation versus average

363 value for both wind speed and wind direction. Some sample values calculated using these

364 polynomials are listed in Table 3. Table 4 lists all the simulation parameters of NOx and $SO_2$

365 that were required.
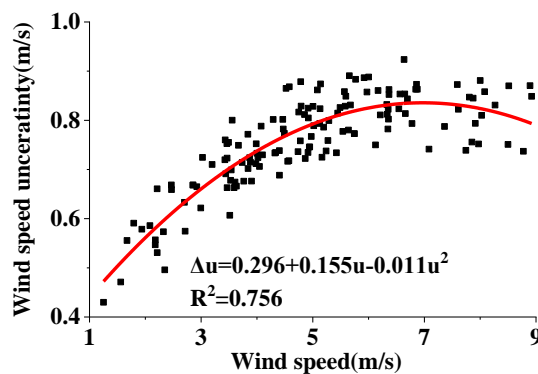
366

367 Figure 4. Polynomial fitting of the uncertainty between wind speed and wind direction.

368    Table 3. Wind speed uncertainty and wind direction uncertainty after polynomial fitting.

| wind speed(m/s) | wind speed uncertainty($\pm$,m/s) |
|---|---|
| 1.2 | 0.466 |
| 2 | 0.562 |
| 3 | 0.662 |
| 4 | 0.740 |
| 5 | 0.796 |
| 6 | 0.83 |
| 7 | 0.842 |
| 8 | 0.832 |

369

370    Table 4. Simulation parameters and data range of NOx and $SO_2$.

| Parameter | Values |
|---|---|
| Emission rate(g/s) | 10, 30, 50, 100 , 150, 200 |
| Wind speed(m/s) | 1.2, 2,3, 4, 5, 6, 7, 8 |
| Measuring distance(km) | 0~10km |
| Sampling resolution | 5~500m, initial integration times $t_{int}$ |
| Fit error(molecules cm$^{-2}$) | $NO_2$: ~$2.5\times10^{15}$; $SO_2$: ~$4\times10^{15}$ |
| Detection limit(molecules cm$^{-2}$) | $NO_2$: $5\times10^{15}$; $SO_2$: $8\times10^{15}$ |
| AMF and its error | 1.15$\pm$10% |
| Gas absorption cross-section errors | $\pm$5% |
| Average atmosphere lifetime | NOx:5h$\pm$1h; $SO_2$: more than 1 day |
| $R_{NOx}$ | $R_{NOx}$ inside the plume is calculated by Eqs. (5), (6), (7) and (8). $R_{NOx}$ in NOx reaction steady-state is 1.32. |

371    The parameters listed in Table 4 were applied in the forward model in order to perform the

372    simulation. The simulation results are shown in Figures 25 and 26 of the Appendix.

373    **4 Analysis of emission flux errors measured by mobile DOAS based on the forward**

374    **model**

375    Figures 25 and 26 in the Appendix show that the modeled relative errors of NOx and $SO_2$

376    emission flux varied with sampling resolution and distance from the point source under dif-

377    ferent wind speeds and emission rates. Some overall features can be derived from these fig-

378    ures. Therefore, typical cases were selected in order to discuss the overall features based on

379 several key factors.

## 4.1 Sampling resolution and its error

381 Sampling resolution variation impacts on the error combination and propagation and its er-

382 ror is an error source.

383 Sampling resolution is derived from GPS records in actual measurement. The typical un-

384 certainty of the GPS readings is <1.5m. For measurements with small sampling resolutions

385 the GPS error can thus cause relatively large uncertainties for the flux contributions from in-

386 dividual measurements (Eq. 1). However, even for small sampling resolutions the GPS errors

387 of neighboring flux contributions almost completely cancel each other. Thus, the contribution

388 of the GPS error to the flux calculation (Eqs. 16 and 17) can be neglected.

389 In actual measurements, if one distance is too long, and this happens to be inside the plume,

390 while the next distance is too short but is already outside the plume, the flux will be overesti-

391 mated in spite of the fact that the sum of the two distances has only a small error. In this case,

392 the sampling error becomes important. The sampling error is largest when the sampling reso-

393 lution is large. Thus a small and uniform sampling resolution is particularly important.

394 In order to discuss the dependence of flux error on sampling resolution, some data were ex-

395 tracted from the Appendix and plotted in Figure 5. This figure shows the increase of relative

396 error with increasing sampling resolution. It should be noted that the smaller the sampling

397 resolution, the more data the mobile DOAS will sample. This directly leads to the inclusion of

398 more data in the emission flux calculations, resulting in the lower emission flux error. How-

399 ever, when far from the source, the plume with narrows quickly (see section 4.2). Appling

400 different sampling resolution is no longer feasible. Therefore, the sampling resolution can on-

401 ly work effectively when the measurements are not far from the source.
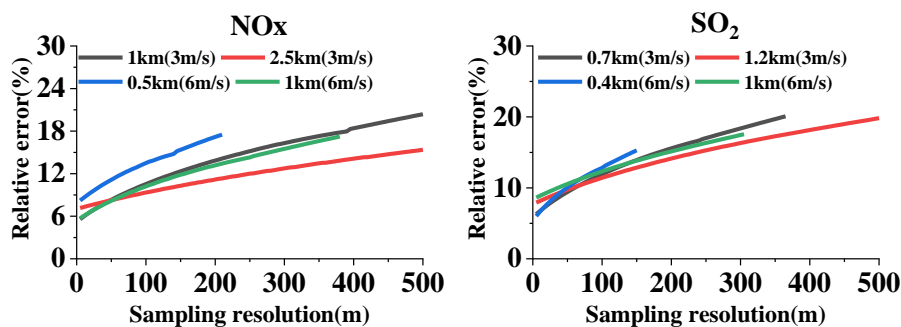
402

403      Figure 5. Dependence of relative errors on sampling resolution (Q = 100 g/s, u = 3 m/s and 6 m/s, at

404                 different measuring distances).

405      The impact of sampling resolution on emission flux error is noticeable. In terms measure-

406 ment efficiency, the sampling resolution should not be too small. Also to avoid large errors

407 and sampling errors, large resolution is not recommended. Therefore, we recommend the

408 proper sampling resolution to be between 5 m and 50 m. Larger resolutions may also be via-

409 ble, but > 100 m is not recommended.

410 **4.2 Measuring distance from the source**

411      Measuring distance is not an error source, but affects the dispersion and NOx chemical re-

412 actions, further adding to the emission flux error. Figure 6 presents typical examples of rela-

413 tive errors varying with distance at a resolution of 20 m. Wind speeds of 3 m/s and 6 m/s were

414 utilized in this example. The overall feature shown in all of the sub-figures of Figure 6 is the

415 rapid decrease and then quick increase of the relative error with measuring distance. Different

416 factors lead to the large errors at small and large distances.

417      First, we analyzed NOx and $SO_2$ emission flux errors for a large measuring distance. The

418 large distance results in the dramatic decrease of SCDs due to dispersion and decay along the

419 plume transport path. The SCDs can be lower than the detection limit of mobile DOAS meas-

420 urements, resulting in a portion of the undetectable flux. Because of dispersion, the plume

421 widths with SCDs above the detection limit and thus the detectable fluxes decrease signifi-

422 cantly with distance, even dropping to zero, as shown in Figure 6. This causes the relative er-

423 ror to increase at large measuring distances.

424      Second, we analyzed NOx and $SO_2$ emission flux errors in the case of a small measuring

425 distance. Figure 6 indicates that the error is large and decreases rapidly with increasing meas-

426 uring distance when close to the source. As discussed in Section 4.1, if more measurement

427 data are included in the calculations of flux, the relative error can decrease. When the meas-

428 uring distance is small, the number of samples can dramatically decrease. For $SO_2$, the rela-

429 tive error can increase significantly when the measurements are close to the point source. For

430 NOx, the relative error is also affected by chemical reactions, this phenomenon that we will

431 discuss in Section 4.4.
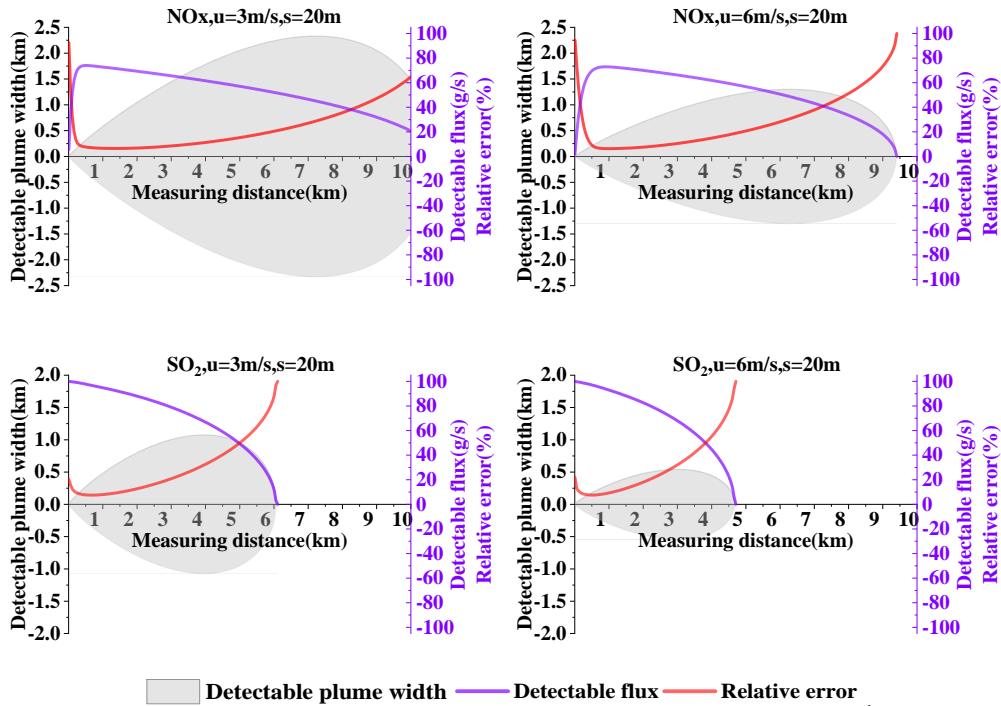
Figure 6. Variation of NOx and $SO_2$ flux relative errors with distance, using Eqs. (16) and (17) (Q = 100 g/s, setting the sampling resolution $s$ = 20 m and the wind speed to 3 m/s and 6 m/s).

**4.3 Wind fields and their uncertainties**

Wind fields can impact both the gas dispersion (Eqs. 2, 9 and 10) and the calculation of emission flux (Eqs. 1 and 15). In terms of dispersion, wind speed affects gas VCD (Eqs. 9 and 10). In terms of flux calculation, the temporal and spatial uncertainty of wind fields can contribute to emission flux calculation errors. Therefore, the effects of wind fields are discussed based on these 2 factors in this section.

Figure 7 displays the variations of the relative errors of NOx and $SO_2$ with wind speed at different distances. The emission rate Q and the sampling resolution are chosen as 100 g/s and 20 m, respectively. Figure 7 indicates the different features of relative error for wind speeds at small and large measurement distances. The relative error of NOx increases with increasing wind speed at different distances, while the $SO_2$ relative error for measurements at small distances exhibits a trend opposite that of the large distance measurements. The causes of the different relationships at small and large measurement distances are discussed in subsection 4.3.1.
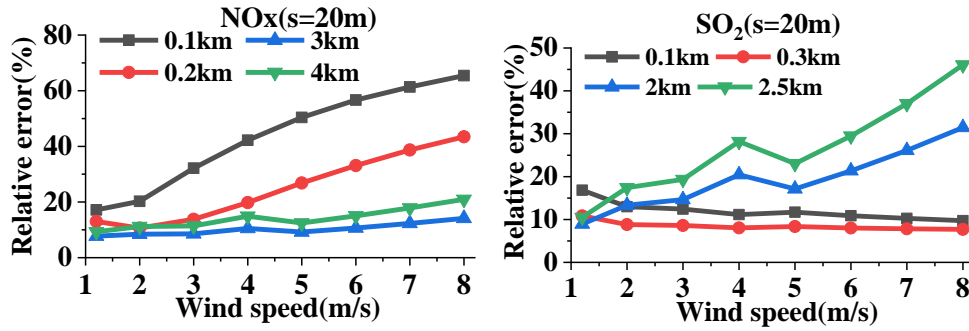
Figure 7. Relative errors of NOx and SO$_2$ emission flux changes with wind speed at different measurement distances (Q = 100 g/s, sampling resolution $s$ = 20 m).

### 4.3.1 Effects of different wind speeds on measurements at small and large measurement distances

Since the NOx and SO$_2$ flux measurement errors of different wind speeds are very different at small and large measurement distances, we discuss them separately.

### 4.3.1.1 SO$_2$

We first analyzed the effect of different wind speeds on the SO$_2$ emission flux error.

Since VCDs decrease with increasing wind speed (Eqs. 9, 10 and 11), more SCDs would be below the detection limit of mobile DOAS at high wind speeds. Hence, the contribution of undetectable SCDs to the error of flux calculations depends on wind speed. In addition, since wind fields are input into the calculations of emission flux (Eqs. 1 and 15), their uncertainties can contribute to the flux measurement error. In order to investigate the contributions of undetectable ambient VCDs and the influence of wind field uncertainties in flux measurement, the ratios $R_{uf}^2$ ($R^2$ of the undetectable flux) and $R_u^2$ ($R^2$ of the wind speed uncertainty) calculated using Eq. (18) are shown in Figures 8c and 8d for different wind speeds and measurement distances.

Again, we first analyzed the measurements at large distances. The undetectable VCDs dominate the effect of wind fields on the error of flux calculations when the measurement distance is large. As shown in Figures 8d, undetectable flux dominates the flux errors when measuring at large distance. The $R_{uf}^2$ becomes greater with larger wind speeds, for large measurement distances. For large measurement distances, as shown in Figures 8c and 8d.

475  Therefore, undetectable VCDs dominate the effect of wind fields on the error of flux calcula-

476  tions when the measurement distance is large. Since VCDs decrease with increasing wind

477  speeds, the flux error associated with undetectable VCDs should be increased with wind

478  speed. This relationship explains the phenomenon that the relative error of emission flux in-

479  creases with increasing wind speed for large measurement distances.

480      Next, the measurements at small distances were analyzed. Figures 8c and 8d indicate that

481  $R^2_{uf}$ is much lower than $R^2_u$ for short measurement distances. The wind field uncertainty

482  dominates the effect of wind fields on the flux calculation errors. Meanwhile, since the rela-

483  tive uncertainty of the wind field decreases with increasing wind speed, the emission flux er-

484  ror decreases with increasing wind speed for short measurement distances, as shown in Figure

485  6.
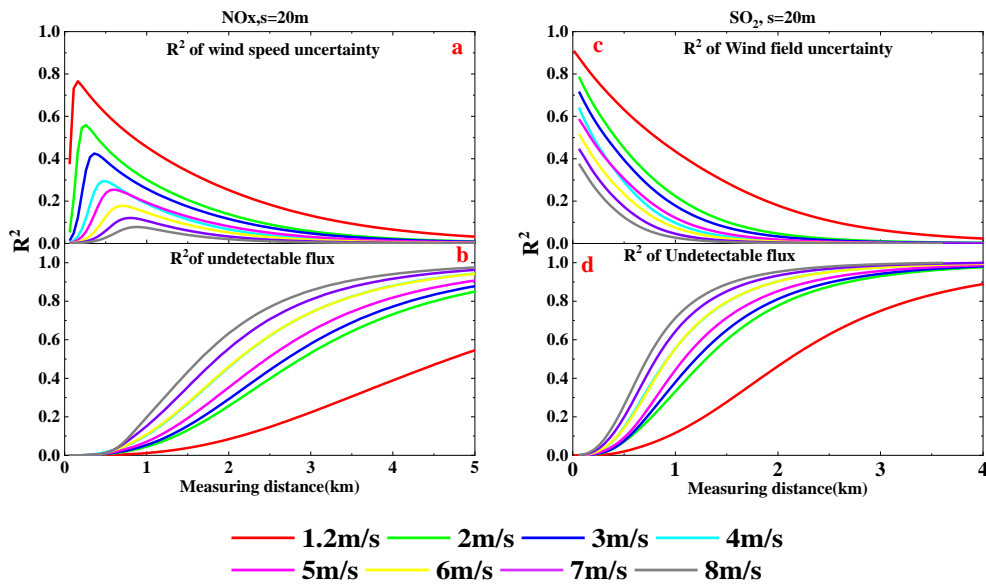
486

487

488     Figure 8. Wind speed uncertainty ratio squared $R^2_u$ (**a** and **c**) and undetectable emission flux ratio squared

489     $R^2_{uf}$ (**b** and **d**) of NO$_2$ and SO$_2$ emission flux measurement error changes with measurement distance for

490                      different wind speeds (Q = 100 g/s, sampling resolution $s$ = 20m).

491

492  **4.3.1.2 NOx**

493      We next analyzed the effect of different wind speeds on NOx emission flux error, as shown

494  in Figures 9a and 9b.

495      The effects of different wind speed dispersions on NOx emission flux error are similar to

496  SO$_2$, i.e., Figures 8b and 8d, indicating that the effects of wind speed dispersion are analogous.

497     The effect of wind field uncertainty is much different from $SO_2$, however, especially when the

498     measurements are very close to the source. When very close, wind field uncertainty influence

499     increases and then decreases with distance. Compared with $SO_2$, the decreasing trend of NOx

500     in the case of far measurement distances is also similar, but the increasing trend is very dif-

501     ferent. This implies that NOx measurements close to the source have another main potential

502     error source, which we will investigate in Section 4.4.

503     The 4 subfigures in Figure 8 share the common characteristic that the $R^2$ lines have inter-

504     sections between 4 m/s and 5 m/s. This implies that the wind field uncertainty effect and the

505     wind field dispersion effect are distinguished between 4 m/s and 5 m/s. In actual measure-

506     ments, undetectable VCDs cannot be well quantified. Therefore, we recommend the proper

507     wind speed for mobile DOAS to be < 4 m/s. The appropriate lower wind speed in this study

508     was 1.2 m/s, But the Gaussian plume model we used becomes increasingly inaccurate when

509     wind speeds are under 1m/s. Thus, we recommend a proper wind speed of 1–4 m/s.

510     **4.3.2 Error budget of undetectable flux, uncertainties of wind speed**

511     The remaining question is what flux error budget is associated with the wind speed. From

512     Section 2.6 we know that Wind field uncertainties mainly come from the wind speed uncertainties.

513     Undetectable flux is the result of SCDs below the detection limit, but the main drivers of $R_{uf}^2$ in-

514     creasing trend along the wind direction is the wind dispersion. Figure 9 presents the changes

515     of $R_u^2$ and $R_{uf}^2$ of NOx and $SO_2$ with distance for different wind speeds, 3 m/s and 6 m/s.

516     As for $SO_2$, the wind field influence contributes most of the emission flux error from wind

517     field uncertainty, in conjunction with wind dispersion. Furthermore, contributions from wind

518     speed uncertainty in the emission flux error are also presented in Figure 9. This demonstrates

519     that wind speed uncertainty dominate the flux error when close measuring.

520     With regard to NOx, the wind speed influence is similar to $SO_2$ when measuring far from

521     the source and very different when measuring close to the source. As discussed above, mobile

522     DOAS can only measure the $NO_2$, as opposed to the NOx. The amount of $NO_2$ yield deter-

523     mines the mobile DOAS measurement result, and thus that of the NOx flux measurement er-

524     ror, especially when measuring very close to the source.
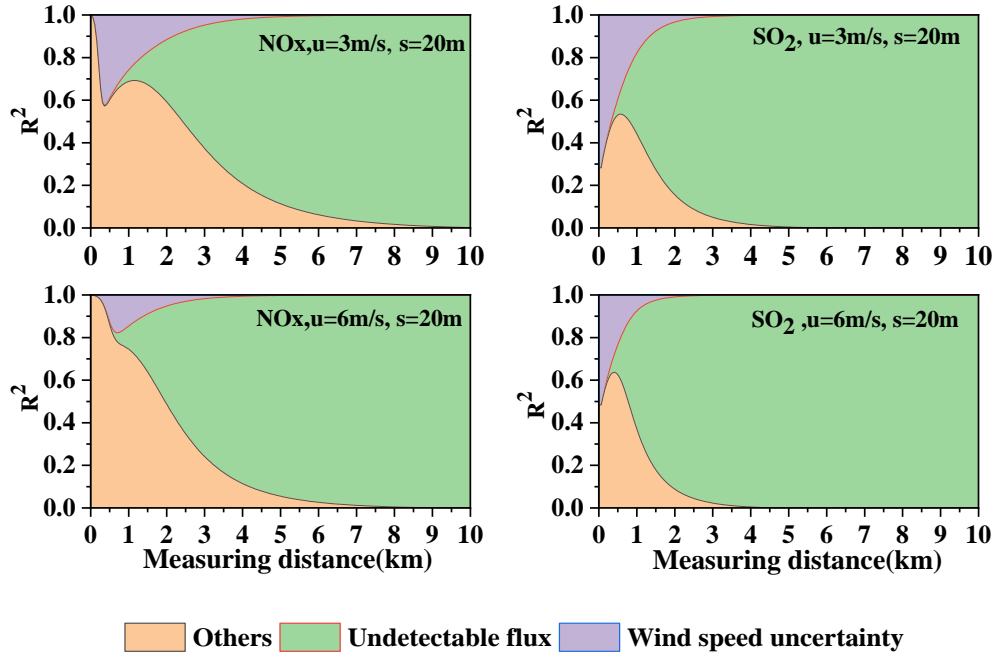
Figure 9. Changes of $R_u^2$ and $R_{uf}^2$ of NOx and SO$_2$ emission flux measurement errors with measurement distance for different wind speeds (Q = 100 g/s).

**4.4 NOx chemical reactions**

In Section 4.2, we left unanswered the question as to why the NOx flux error is very large when very close to the source (see Figure 6). In this section, we will investigate the reason for this phenomenon.

Stacks mainly exhaust NO, which then transforms into NO$_2$ in a few minutes due to chemical reactions. Since NOx disperses along the wind direction, this means that the [NOx]/[NO$_2$] ratio varies with distance. With O$_3$ mixing to the air parcels of the plume continually, more NO$_2$ would yield and [NOx]/[NO$_2$] ratio decreases with the distance before the NOx reaction steady-state. For readability, we here show the increasing trend of [NO$_2$]/[NOx] ratio along the distance in Figure 10a.

In actual measurements, especially for elevated point sources, the dependence of the [NOx]/[NO$_2$] ratio on the distance from the air parcels of the plume is difficult to measure. The [NOx]/[NO$_2$] ratio could e.g. be measured by an in situ instrument on the ground. However, in some cases the plume might not reach the ground. And even if it reaches the ground the measured [NOx]/[NO$_2$] ratio is probably not representative for the whole plume. Furthermore, also the ambient [O$_3$] could be measured, which would help to constrain the

545 [NOx]/[NO$_2$] ratio. But also if O$_3$ measurements are available, the calculation of the

546 [NOx]/[NO$_2$] ratio will have its uncertainties, and the derived [NOx]/[NO$_2$] ratio will again

547 not be representative for the whole plume. Thus in our study, we calculate the [NOx]/[NO$_2$]

548 ratio based on the dispersion model with some additional assumptions which are outlined in

549 the text. In this way we can derive the general dependencies of the [NOx]/[NO$_2$] ratio on the

550 plume distance and apply a corresponding correction. However, for the NOx flux calculations,

551 even after the application of the [NOx]/[NO$_2$] ratio correction factor, substantial flux errors

552 near the source might occur.

553  Subfigure b in Figure 10 displays the $R^2_{RNOx}$ value of the [NOx]/[NO$_2$] ratio correction error.

554 The larger the [NOx]/[NO$_2$] ratio, the larger the $R^2_{RNOx}$ value of the [NOx]/[NO$_2$] ratio cor-

555 rection. This causes the $R^2_{RNOx}$ to increase, to as high as 1, when near the source. Also, from

556 the $R^2_{RNOx}$ value we discovered that the [NOx]/[NO$_2$] ratio correction error is the main error

557 source when close to the emission source. Hence, the main flux error source near the emission

558 source is the [NOx]/[NO$_2$] ratio correction error.
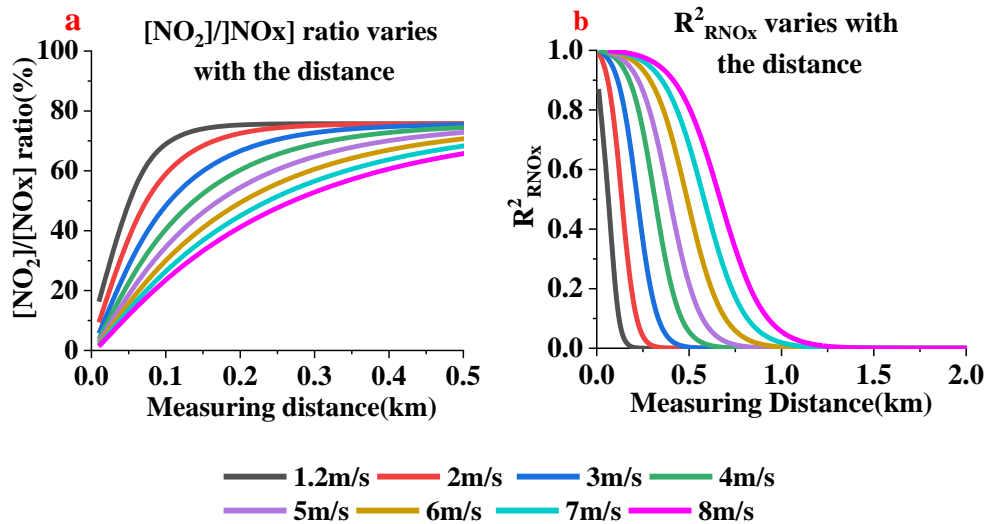
559

560

561 Figure 10. variation of [NO$_2$]/[NOx] ratio (**a**) $R^2_{RNOx}$ with distance (**b**) at different wind speeds (Q = 100

562                     g/s).

563  Since we know that the [NOx]/[NO$_2$] ratio correction error is the main error source near the

564 emission source, developing ways to avoid or minimize this error is our goal.

565    In real-world experiments, accurately measuring NOx flux requires NOx to reach a

566    steady-state. According to Eq. (3), when time approaches infinity, the $NO_2$ reaction rate $r_{NO2}$

567    approaches 0, indicating that NOx reaches a steady-state. In theory, steady-state NOx is an

568    ideal condition for measuring NOx flux. Infinite time, however, is not our expectation. If we

569    regard $r_{NO2} = 0.05 r_{max}$ as the approached steady-state, the approached steady-state time could

570    be attained, as well as the approached steady-state distance. $r_{max}$ is defined as the theoretical

571    $NO_2$ maximal reaction rate, which is $r_{NO2} = k_5 [NO]_0 [O_3]$. Figure 11a displays the variation of

572    $\dfrac{r_{NO2}}{r_{max}}$ with time and Figure 11b displays the approached steady-state distance.

573    In order to investigate the feasibility of our recommendation, we used the following equa-

574    tion for analysis:

$$E_{RNOx} = \frac{\Delta F_{RNOx}}{DQ} \times 100\% \tag{19}$$

576    where $\Delta F_{RNOx}$ is the flux error resulting from the [NOx]/[$NO_2$] ratio correction at the ap-

577    proached steady-state distance. $E_{RNOx}$ is used rather than $R^2$ because $R^2$ only represents the

578    error source contribution/budget. For example, the $R^2$ value of the [NOx]/[$NO_2$] ratio correc-

579    tion error is 0.9, while the total relative error is only 10%. In this case, it seems that we cannot

580    accept the high $R^2$, although the total relative error is acceptable. Therefore, in our judgment,

581    using $E_{RNOx}$ is an advantage.

582    The $E_{RNOx}$ values at the approached steady-state distance for different wind speeds and

583    emission rates were calculated, and the results are presented in Figure 11c. From this figure,

584    we can infer that $E_{RNOx}$ is approximately 5%, which is very low. This indicates that the flux

585    error resulting from the [NOx]/[$NO_2$] ratio correction at the approached steady-state distance

586    is very small and can thus be regarded as negligible.
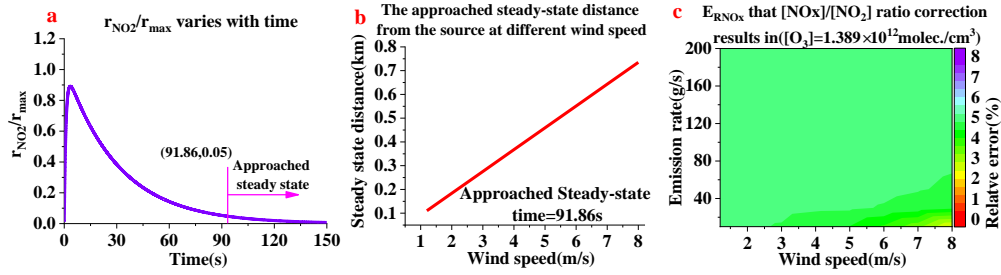
587

588     Figure 11. variation of $r_{NO2}/r_{max}$ with time (**a**), NOx steady-state distance from the source (**b**) and $E_{RNOx}$

589         values (**c**) under different emission rates and wind speeds ([$O_3$]= $1.389 \times 10^{12}$ molecules cm$^{-3}$).

590     According to Eq. (3), $r_{NO2}$ depends on [$O_3$]. Hence, we also calculated the NOx

591 steady-state distance and $E_{RNOx}$ under different [$O_3$]. The $E_{RNOx}$ was also approximately 5%

592 under different [$O_3$], as shown in Figure 12. The dependence calculation demonstrates that

593 $E_{RNOx}$ is also very small under different [$O_3$]. Consequently, regarding $r_{NO2} = 0.05 r_{max}$ as the

594 approached steady-state seems to be acceptable.
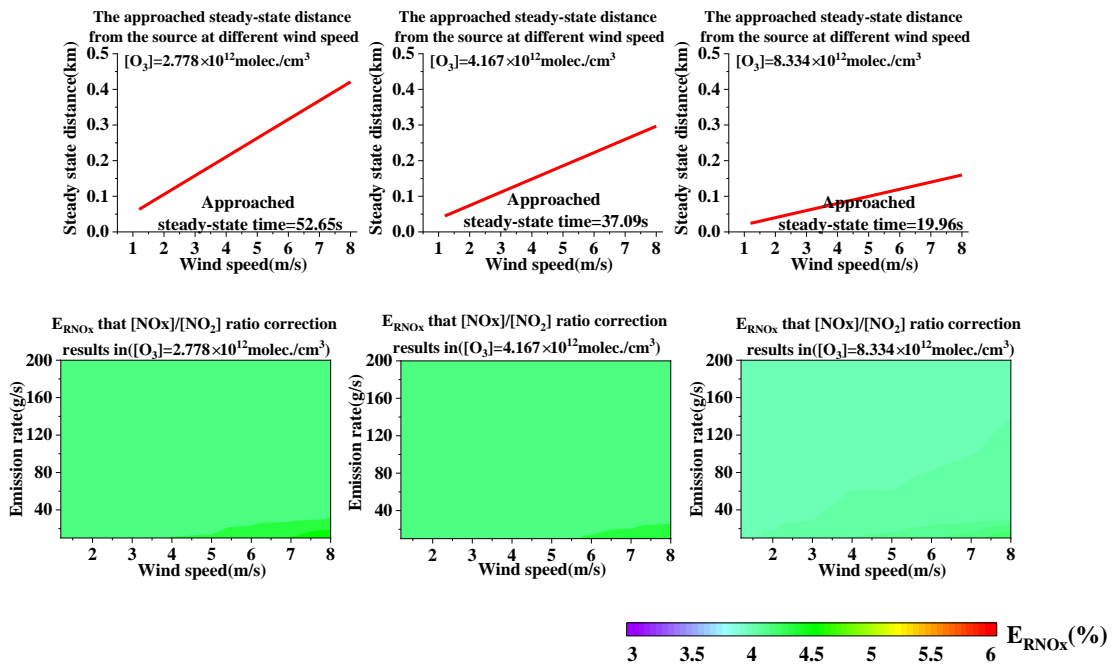
595

596

597

598     Figure 12. NOx approached steady-state distance from the source (upper plot) and $E_{RNOx}$ values (bottom

599         plot) under different emission rates, different wind speeds, and different [$O_3$].

600     In summary, when very close to the emission source, the main flux error source is the

601 [NOx]/[$NO_2$] ratio correction error. In order to avoid or minimize this error, we recommend

602 $r_{NO2} = 0.05 r_{max}$ as the approached steady-state, in which case the approached steady-state

603 distance is the starting measurement distance. The overall distances for different [O$_3$] concen-

604 trations were also simulated as a reference for the DOAS measurement of NOx point source

605 emissions, as shown in Figure 13.
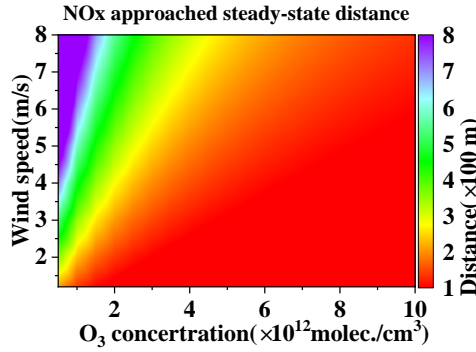
607 Figure 13. NOx steady-state distance from the source for different [O$_3$] concentrations ($r_{NO2} = 0.05r_{max}$).

609 **4.5 Undetectable flux**

610 As discussed in sections 4.3, undetectable flux dominates the flux error when far from

611 source. In the following, we discuss further details of the undetectable flux error. The unde-

612 tectable flux is caused by SCDs below the detection limit. Following Platt and Stutz (2008),

613 we set the detection limit as 2 times the fit error. While the exact value of the detection limit

614 might be different for different instruments and measurement conditions, we use this value to

615 derive the general dependencies of this error term and its contribution to the total flux error.

616 VCDs are sensitive to wind speeds and the dispersion (Eqs. 9 and 10), so is the undetecta-

617 ble flux. We calculate the undetectable flux and its $R_{uf}^2$ along wind direction (equal to along

618 the measuring distance) as shown in Figure 14 (for an emission rate of 100 g/s). As discussed,

619 the main driver of undetectable flux increasing trend along the wind direction is attributed to

620 the wind dispersion as can be seen from Figure 14. With measuring distance far away, the un-

621 detectable flux gradually dominates the flux error which can be denoted by $R_{uf}^2$ trend. Large

622 wind speed also results in quick dispersion thus leads more undetectable flux. The $R_{uf}^2$ and

623 the undetectable flux increases rapidly under the wind speed of 8 m/s than that of 1.2 m/s for

624 both NOx and SO$_2$.
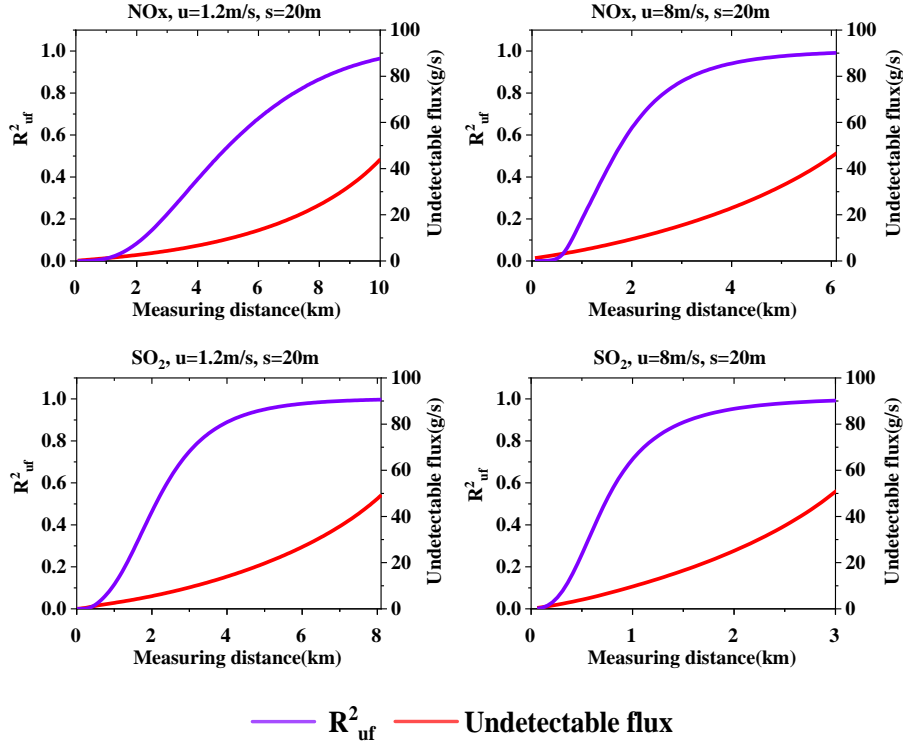
625

626

627

Figure 14. NOx and SO$_2$ absolute flux error, and the $R_{uf}^2$ that Undetectable SCDs result in (Q = 100 g/s).

## 4.6 Gas absorption cross-section error

As discussed in section 2.6, the gas absorption cross-section error contribution to SCD errors is independent of the SCD fit error. Uncertainties of the trace gas cross-sections cause systematic SCD uncertainty. We calculated $R_{cro}^2$ along the wind direction and the total relative errors at the speed of 1.2m/s and 8m/s, as shown in Figure 15. The $R_{cro}^2$ variation trend is similar to $R_{uf}^2$ in section 4.6 due to the relative error variation. However, maximum $R_{cro}^2$ has subtle difference but varies apparently along the wind direction under different wind speed, which indicates that $R_{cro}^2$ is not very sensitive to wind speeds but sensitive to the dispersion. From Figure 15 we see that $R_{cro}^2$ could approach 0.5, which means that gas cross-section error might even become the main error source. However, when $R_{cro}^2$ is close to 0.5, the relative errors of NOx and SO$_2$ are at low levels. This further suggests the trace gas cross-section error has an overall small contribution to the total flux error.
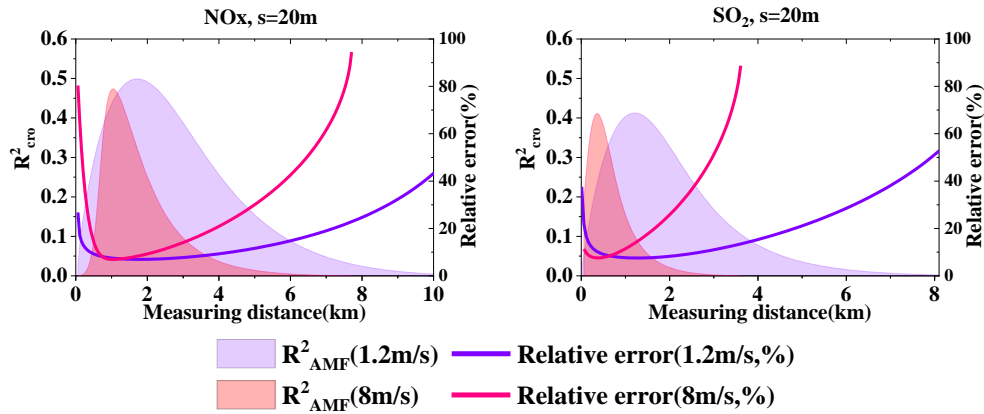
644    Figure 15. NOx and SO$_2$ $R^2_{cro}$ of absorption cross-section error under different wind speed (Q = 100

645    g/s).

646    **4.7 AMF error**

647    AMF values depends on plume height, SZA and aerosol optical density (AOD) as shown in

648    Figure 16. For plume heights < 50m, the AMF is around 1.03 and its error can be neglected.

649    For plume heights $\cong$ 250m, the AMF error is about $\pm$10%. Since the plume height in our

650    study is about 250m, the contribution from the AMF error has to be taken into account.

651    Since VCDs are derived from SCDs by dividing the AMF, then AMF errors introduce VCD

652    errors, which furthermore contribute to the emission flux errors. Wind speed uncertainty is the

653    main error source when close to the source. With larger wind speed, the relative error of the

654    wind speed becomes smaller which then also contributes less to the flux error. This indicates

655    that the flux error that results from other error sources, such as the AMF error, have larger rel-

656    ative contributions under larger wind speed. Figure 17 presents $R^2_{AMF}$ and the total relative

657    errors for wind speeds of 1.2 m/s and 8 m/s. From Figure 17 we could see that $R^2_{AMF}$ for SO$_2$

658    under the speed of 1.2 m/s is very small while it becomes larger at the speed of 8m/s, even

659    near 0.5 when near the source. The NOx flux error, however, is less affected by the AMF error

660    for $R^2_{AMF} < 0.1$.
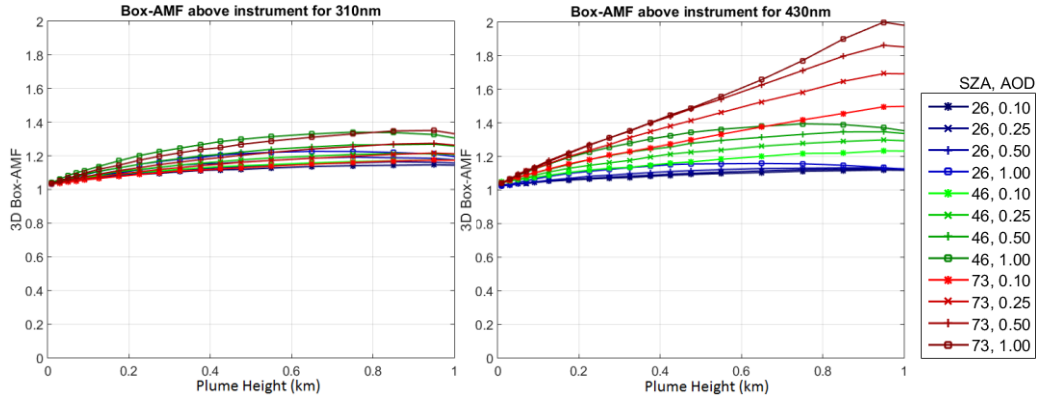
Figure 16. 3D Box-AMF dependence on plume height, SZA and aerosol optical density (AOD) for 310nm and 430nm. For the aerosols a box profile between the surface and 1km was assumed.
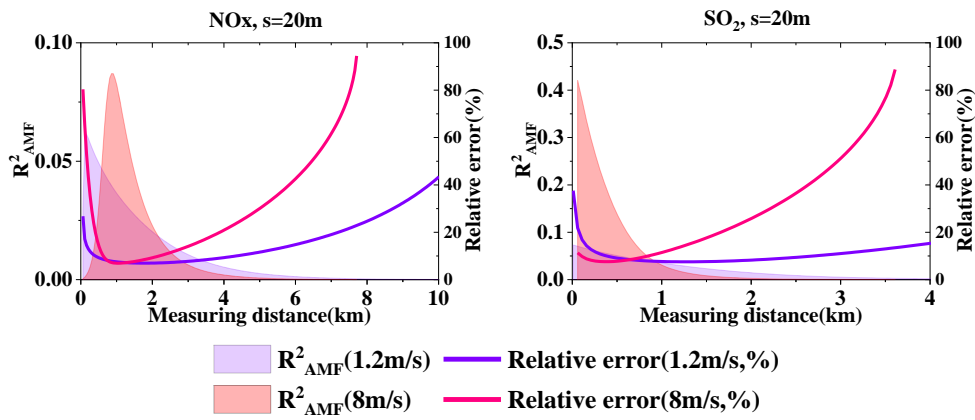
Figure 17. NOx and SO$_2$ total relative error, $R^2_{AMF}$ of AMF error under different wind speed (Q = 100 g/s, s=20m).

## 4.8 Effect of number of measurement times

In our experiments, we only simulated a single scan of the plume by the mobile DOAS at each specific distance. In reality, we usually scan the plume cross-section several times in order to reduce the flux error. The elapsed time between two scans at the same distance from the source is then also an important parameter. The more of the elapsed time, the greater the uncertainties due to temporal variations of the flux and/or the wind fields are likely to be. Here, we assumed that the elapsed time is small and its influence can thus be neglected in our simulation. Figure 18 displays the simulation example of NOx and SO$_2$ flux error under different measurement times.

The error sources of the emission flux can be classified into 2 types. The first is the measurable error/uncertainty: wind speed uncertainty, AMF error and undetectable flux. The sec-

680  ond is: [NOx]/[NO$_2$] ratio correction error near the source and the gas absorption

681  cross-section error. The flux error resulting from the first type of error source can be lowered

682  by scanning the plume more times while the second cannot. Undetectable SCDs result in un-

683  detectable flux, and it can be reduced by more measurements times in theory. In reality, this is

684  often not possible because it requires that all measurement conditions (e.g. the wind field or

685  the background concentrations) stay unchanged. This means that the undetectable flux is hard

686  to be lowered by more time scanning in the actual measurements, although it can be easily

687  realized in theory. Therefore, in practice also the undetectable flux error belongs to the second

688  type of errors, which cannot be reduced by multiple measurements.

689      According to the analysis in Section 4.3, the undetectable flux is the main error source

690  when far from the emission source. Consequently, the flux error under different numbers of

691  scans for both NOx and SO$_2$ cannot be significantly lowered when measuring far from the

692  source (range D in Figure 18). Within the close measurement range (range C in Figure 18),

693  the first type of error source is the predominant source of SO$_2$ error, and thus the flux error can

694  be lowered by additional plume scans. For NOx, however, the [NOx]/[NO$_2$] ratio correction

695  error is the main error source when very close to the emission source (range A in Figure 18),

696  and thus the effect of additional plume scans is not evident. A little farther from the source,

697  the first type of error source becomes the main error source (range B in Figure 18). Ultimately,

698  the impact of additional plume scans becomes effective.
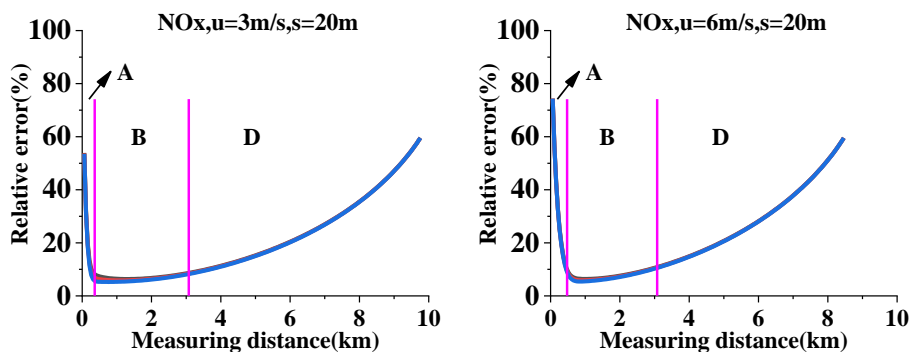
699
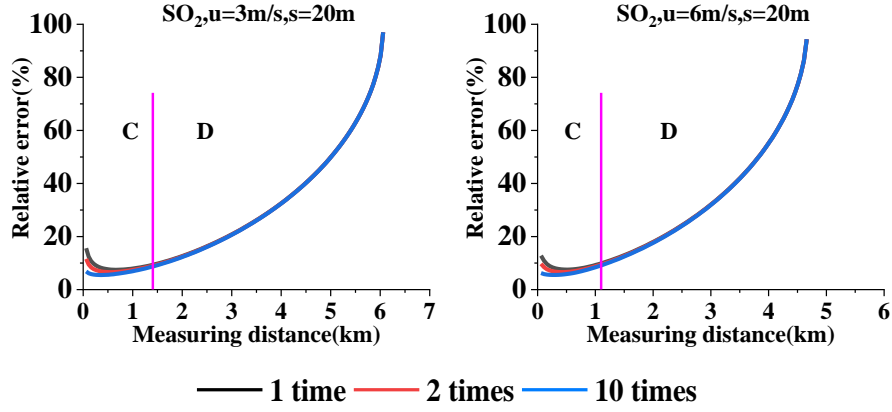
Figure 18. Emission flux error under different numbers of scans. Range A is very close to the source, range B is not too close or too far, range C is close to the source, and D is far from the source (Q = 100 g/s).

**4.9 Effect of spectrometer integration times**

Spectrometer noise is the main noise source of the mobile DOAS instrument (Platt and Stutz, 2008; Danckaert et al., 2015). The noise level varies under different integration times, thereby changing the fit error and detection limit, which would then affect the flux measurement error. Therefore, this section is focused on the effect of spectrometer integration times on mobile DOAS flux measurement error.

The relationships among fit error, detection limit, and noise level are (Kraus, 2006; Platt and Stutz, 2008)

$$SCD_{fit} \propto Fit_{err} \propto \sigma, \quad D_{\lim} \propto \sigma \tag{20}$$

where $SCD_{fit}$ is the $SCD$ fitting error, $Fit_{err}$ is the residual in DOAS fitting, $D_{\lim}$ is the detection limit, and $\sigma$ is the noise level. The noise level is approximately inversely proportional to the square root of the integration times.

The sampling resolution of mobile DOAS can be expressed as:

$$s = v \cdot (t_s \cdot n) = v \cdot t_{int} \tag{21}$$

where $v$ is the car speed, $t_s$ is a single integration time of the spectrometer, $n$ is the spectrometer averaging times, and $t_{int}$ is the spectrometer integration times.

According to Eq. (21), the effect of integration times can be investigated in 2 different ways: Varying the car speed and thus fixing the sampling resolution or fixing the car speed and thus

723    varying the sampling resolution. In this study, we simulated the integration times for $0.25\,t_{int}$,

724    $0.5\,t_{int}$, $1\,t_{int}$, $2\,t_{int}$ and $4\,t_{int}$.

**4.9.1 Prescribed sampling resolution**

726    Since different integration times results in the car speed varying in a large range that car

727    speed cannot be fully realized in actuality at a given sampling resolution, the sampling resolu-

728    tion cannot be too small. Here, we chose a 50 m sampling resolution as a case study.

729    Figure 19 displays the relative error under different integration times at a given sampling

730    resolution (Q = 100 g/s). From Figure 19 we can see the relative error differences resulting

731    from various integration times.

732    Since a larger integration times will directly lead to a lower detection limit and a smaller

733    fitting error, and indirectly to a lower undetectable flux and a lower fit error, the relative error

734    nonlinearly decreases with increasing integration times. Since the relative error differences

735    caused by integration times become more evident when far from the source (range B in Figure

736    19), our analysis focused on this range. This phenomenon is due to that fact that different in-

737    tegration times mainly act on the fit error and the detection limit. Therefore, we separately

738    analyzed these 2 error sources.
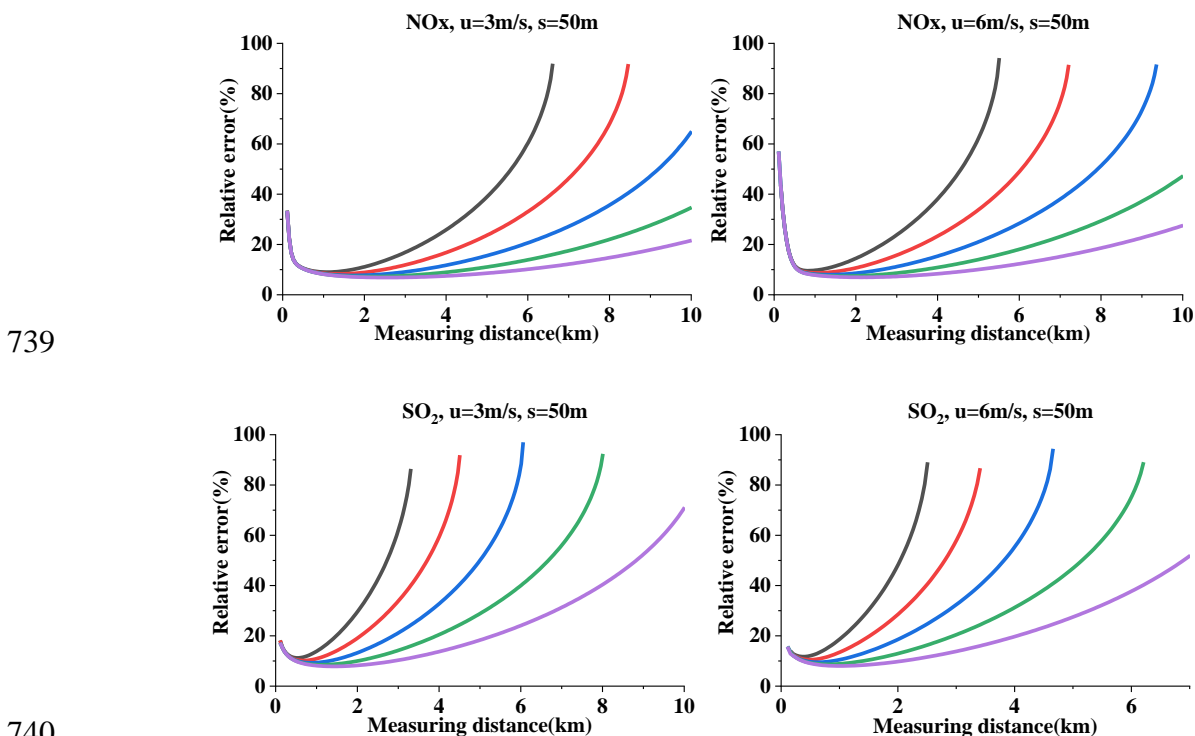
742 Figure 19. Relative error under different integration times at a prescribed sampling resolution (Q = 100

743 g/s).

744     We analyzed the undetectable flux differences resulting from different detection limits.

745 Figure 20 presents the undetectable flux and its $R^2$ values. From the $R^2$ values we could infer

746 that undetectable flux contributes most to the error when far from the source. Especially for

747 smaller integration times, undetectable flux $R^2$ increases very quickly with distance. In addi-

748 tion, the variation trend of undetectable flux when far from the source corresponds to the rela-

749 tive error trend. Therefore, we infer that the relative error trend under different integration

750 times is determined by the undetectable flux.

751     In brief, different integration times significantly impact the relative error at a given sam-

752 pling resolution when far from the source, and these error differences are mainly attributed to

753 the undetectable flux differences resulting from the detection limit.

754 .

755

756

757
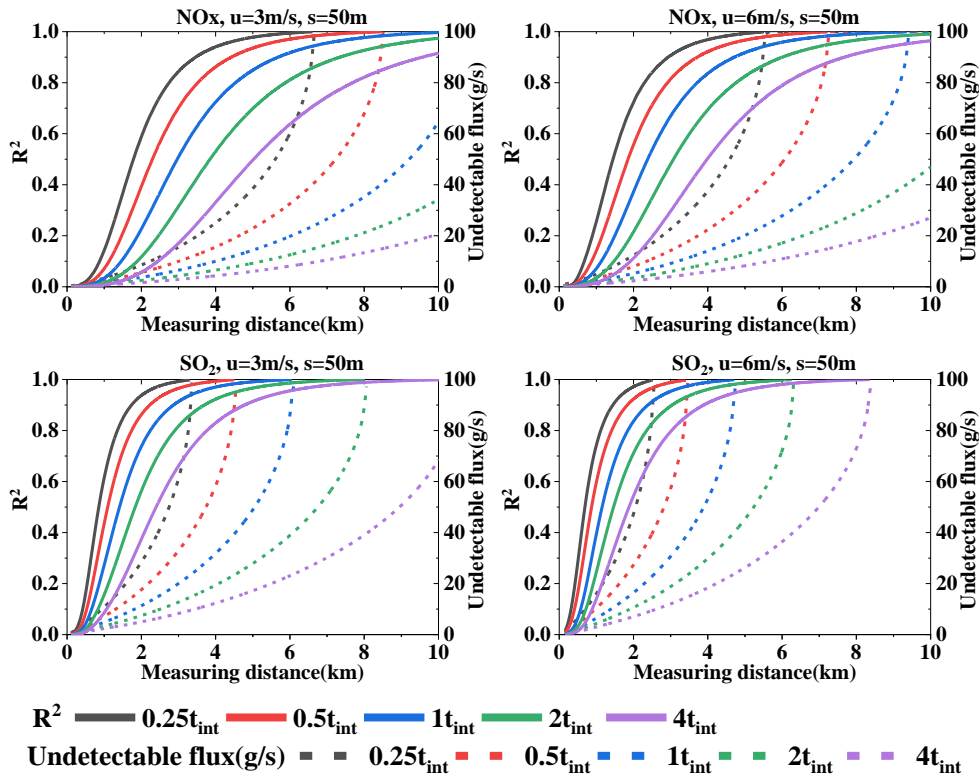
758 Figure 20. Undetectable flux and its $R^2$ values under wind speeds of 3 m/s and 6 m/s for NOx and SO$_2$

759 under different integration times. The sampling resolution is 50 m (Q = 100 g/s).

760 **4.9.2 Prescribed car speed**

761     When the car speed is prescribed, the sampling resolution is determined by the integration

762 times. Therefore, an effect on the error due to the sampling resolution would be introduced

763 (Section 4.1).

764  Figure 21 presents the relative error under different integration times at a given car speed. It

765 is interesting that the relative error differences caused by integration times in ranges B and D

766 (NOx) are opposite those of ranges C and D ($SO_2$). We have analyzed the causes of the rela-

767 tive error differences in range D, but did not analyze the causes in range B or C.

768  From Section 4.1 we know that, within the proper resolution range, the relative error in-

769 creases with increasing sampling resolution. Moreover, the sampling resolution can only af-

770 fect the first type of error source mentioned in Section 4.6, i.e., the wind speed uncertainty,

771 and AMF error. We calculated the sum of the $R^2$ values for the wind field uncertainty, and fit

772 error. In addition, the sum of the absolute flux errors introduced by these error sources is

773 shown in Figure 22. The $R^2$ values indicate that, in range B or C, these factors are the main

774 error source and thus cause the differences under different $t_{int}$. The flux error trends do not

775 all correspond to the relative error trend due to the undetectable flux, although it is still the

776 main error source that determines the differences in range B or C.

777  Furthermore, we can conclude that the different integration times that significantly affect

778 the relative error at a given car speed can be divided into 2 ranges: B and D for NOx, and C

779 and D for $SO_2$. In range B/C, the differences under different $t_{int}$ can be attributed to the

780 sampling resolution effect. In range D, the differences under different $t_{int}$ can be attributed

781 to the undetectable flux.

782

783
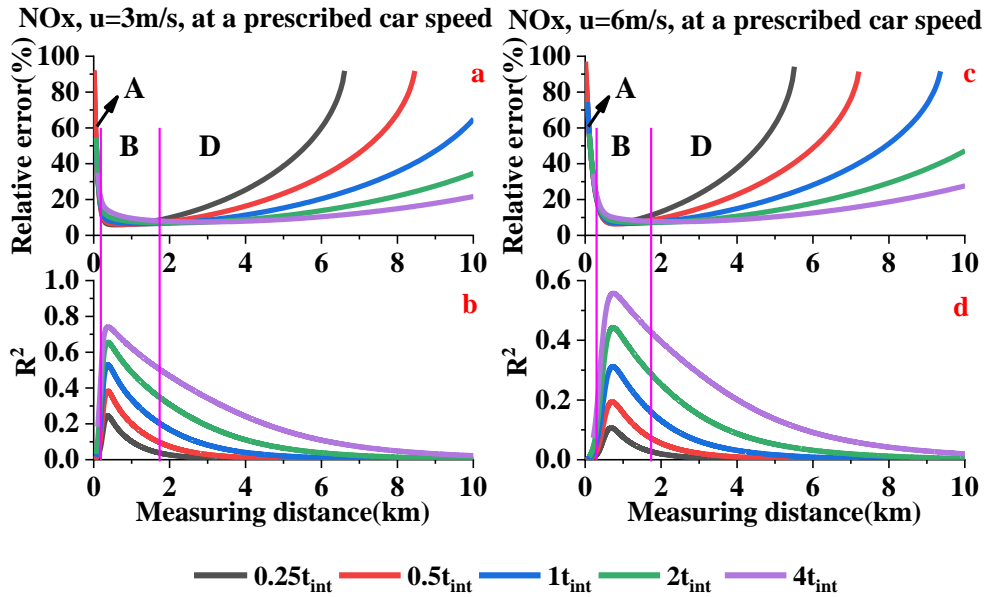
Figure 21. NOx relative errors (**a** and **c**), $R^2$ values introduced by the wind field uncertainty AMF error (**b** and **d**)(Q = 100 g/s).

786

787
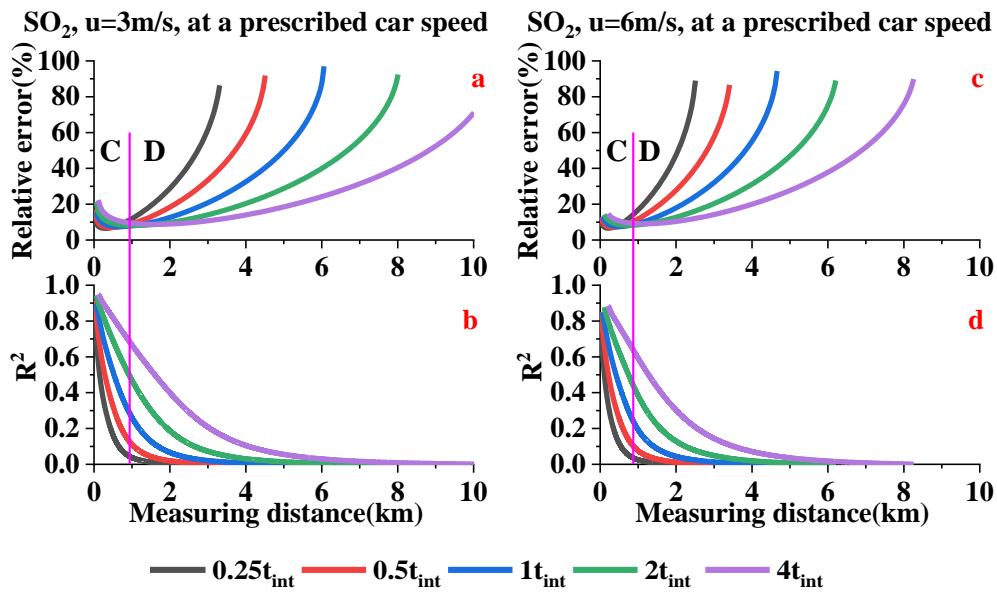
Figure 22. SO$_2$ relative errors (**a** and **c**), $R^2$ values, and flux errors introduced by the wind field uncertainty and AMF error (**b** and **d**) under wind speeds of 3 m/s and 6 m/s (Q = 100 g/s).

790

Different integration times result in different fit errors and different detection limits. The analysis in terms of either a given sampling resolution or a given car speed has significant implications. For example, when measuring close to the source, i.e., range B or C in Figures 21 and 22, we can fix the car speed within a proper low integration times in order to obtain a higher resolution, which indirectly results in a lower error. When measuring far from the source, proper large sampling resolutions are available since the main error source is the un-

797    detectable flux. This further suggests that larger integration times and higher car speeds can

798    be applied in order to increase the efficiency of measuring flux.

799    **4.10 Effects from other factors**

800    Measuring emission flux is extremely complex. It is feasible to analyze the error caused by

801    some key factors, but it is also necessary to study other factors.

802    **4.10.1 Emission rate**

803    Emission rate is an objective factor. The simulation results suggest that the emission rate

804    significantly affects the relative error distribution. Therefore, disregarding the emission rate in

805    order to analyze the error is a less rigorous approach.

806    From Eqs. (9), (10), and (11) we know that $VCD(x,y)$ is proportional to the emission rate,

807    which means that lower emission rates generate lower $VCD(x,y)$, leading to a reduction of the

808    measurable plume width with SCDs above the detection limit. Ultimately, this results in larger

809    emission flux errors at the same distance when the emission rate is low, even if there is no

810    proper resolution to measure. In order to achieve a low emission flux error, emission rates that

811    are too low are not recommended. We cannot provide a precise lower limit for the emission

812    rate, but can propose a range of values. From the figures in the Appendix, we can see that the

813    red areas (indicating large errors) cover nearly all of the figure when the NOx emission rate is

814    < 30 g/s and the $SO_2$ emission rate is < 50 g/s. Therefore, emission rates < 30 g/s for NOx and

815    < 50 g/s for $SO_2$ are not recommended in mobile DOAS measurements.

816    **4.10.2 Different source heights**

817    The mobile DOAS height, which is approximately 2 m from the ground to the telescope, is

818    usually negligible in actual measurements. When the source is not very high, however, more

819    gas will descend to the ground under the mobile DOAS telescope, where it cannot be meas-

820    ured. Here, we simulated the emission source at heights of 10 m, 20 m, 50 m, 100 m, and 200

821    m. Since lower wind speeds will lead to gas quickly descending to the ground, we simulated a

822    low wind speed of 3 m/s. The emission rate was set to 100 g/s.

823    The lower the source height, the more gas will descend to the ground, resulting in changes

824    to the undetectable flux. Figure 23 displays the undetectable flux of NOx and $SO_2$ for the

825 wind speed of 3 m/s. From this figure we can see that obvious variations occur in the NOx

826 and SO$_2$ undetectable flux when close to the source. The undetectable flux variation may im-

827 pact the flux relative error.

828     Figure 24 presents the flux relative error at different heights. These results show that the

829 relative errors of NOx and SO$_2$ exhibit little variation. This is because, compared to the flux

830 error resulting from other main error sources, the undetectable flux variation with height is

831 negligible.
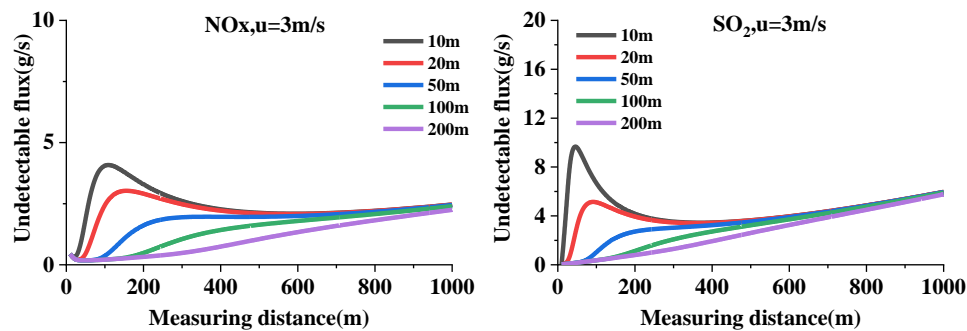
832
833     Figure 23. NOx and SO$_2$ undetectable flux values at different source heights (Q = 100 g/s, u = 3 m/s).
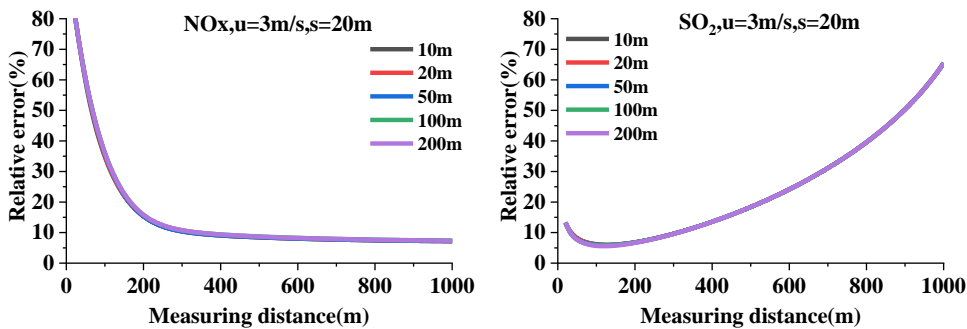
834
835     Figure 24. NOx and SO$_2$ flux relative errors at different source heights (Q = 100 g/s, u = 3 m/s, *s* = 20 m).

836 **4.10.3 Uncertainties of the Gaussian dispersion model**

837     The Gaussian dispersion model was assumed in the forward model during our discussion of

838 the emission flux error budget. The dispersion in actual measurements, however, depends on

839 meteorological conditions and surrounding terrain. Also a non-Gaussian behavior of the

840 plume and vertical wind shear might contribute to the total flux error. Thus, the results of this

841 study should be seen as a lower limit of the total flux errors. In some cases, for NO$_2$, also the

842 stratospheric absorption might become important. However, this might only happen for very

843 long measurement durations or for measurements at high SZA. Differences in the Gaussian

844 dispersion model from reality could have resulted in a bias of the error budget presented in

845    this study from reality. The investigation of the detailed of the dispersion model is outside the

846    scope of this investigation.

847    **5 Conclusions**

848    In this study, we used a Gaussian dispersion model to quantify the NOx and $SO_2$ point

849    source emission flux errors of mobile DOAS.

850    We first established a forward model for the simulation.

851    In the forward model, we modified the Gaussian dispersion model in order to make it ap-

852    propriate for the DOAS technique, i.e., the $SO_2$ and NOx VCD dispersion model. The NOx

853    VCD dispersion model also took NOx atmospheric chemical reactions into consideration.

854    Second, we analyzed the simulation data, reaching the following conclusions:

855    (**1**) The impact of sampling resolution on emission flux error is noticeable. Smaller resolu-

856    tion can lower the flux error. In terms of measurement efficiency, the sampling resolution

857    should be moderate. Therefore, we recommended the proper sampling resolution to range

858    from 5–50 m. Larger resolutions could also be applied, but > 100 m is not recommended.

859    (**2**) Measuring distance significantly affects the flux measurement error. When far from the

860    source, undetectable flux from the wind dispersion effect, which results in large errors, will be

861    noticeable. When close to the emission source, a low number of sampling data leads to large

862    flux errors. The proper measuring distance is not too far or too close to the source. Due to the

863    complex situation, the proper distance is difficult to quantify. It should be noted that unde-

864    tectable flux is the error source which was not considered in (Johansson et al., 2008, 2009;

865    Rivera et al., 2009, 2012; Ibrahim et al., 2010; Shaiganfar et al., 2011, 2017; Berg, et al.,2012;

866    Walter, 2012 et al.; Wu et al., 2013, 2017; Frins et al., 2014; Merlaud et al., 2018).

867    (**3**) The wind field influence could be classified into 2 parts: uncertainty and dispersion.

868    Dispersion is more evident when far from the emission source; thus, undetectable flux is the

869    main error source for both $SO_2$ and NOx. When measuring close to the emission source, wind

870    field uncertainty is the main error source of $SO_2$ flux measurements, but not of NOx. For

871    higher wind speeds, the dispersion effect is more distinct, thereby directly leading to more

872    undetectable flux. We recommended a wind speed of 1–4 m/s for accurate mobile DOAS

873     measurements.

874     **(4)** NO converts to $NO_2$ upon exhaust from a stack and reaches the NOx steady-state within

875     a few minutes. During this time period the [NOx]/[$NO_2$] ratio decreases continuously with

876     distance, resulting in a flux error due to [NOx]/[$NO_2$] ratio correction. Our simulation indi-

877     cates that [NOx]/[$NO_2$] ratio correction is the main error source when measuring very close to

878     the emission source. To minimize the large [NOx]/[$NO_2$] ratio correction error, we recom-

879     mended $r_{NO2} = 0.05 r_{max}$ as the NOx steady-state. Therefore, the proper starting measurement

880     distance for NOx could be determined, which we displayed in Figure 13.

881     **(5)** The undetectable flux is sensitive to wind speeds and wind dispersion.

882     **(6)** The AMF error is not the main error source for NOx; for $SO_2$ it can only become im-

883     portant for measurements close to the source and for high wind speeds.

884     **(7)** The gas absorption cross-section error might become the main error source when at low

885     levels but in such conditions the absolute flux error is rather small.

886      **(8)** Repeating the measurements several times can only affect the measurable error source,

887     and do not affect the unmeasurable. This causes the $SO_2$ flux error to decrease when not very

888     far from the emission source. As for NOx, increasing the number of measurement times could

889     become effective when not very close to the source but not too far away.

890     **(9)** Different integration times result in different fit errors and detection limits. For a pre-

891     scribed sampling resolution, relative error differences under different integration times are

892     attributed to undetectable flux differences caused by the detection limit, especially for distant

893     measurements. For a prescribed car speed, the sampling resolution effect is introduced. When

894     measuring not very far from the emission source, the relative error differences are attributed

895     to the sampling resolution effect from the first type of error source. Far from the source, the

896     detection limit applies.

897     **(10)** Other studies have indicated that emission rates < 30 g/s for NOx and < 50 g/s for $SO_2$

898     are not recommended in mobile DOAS measurements. The source height exerts an impact on

899     the undetectable flux, but has little impact on the total error.

900     The advantage of the method put forth in this study is that many scenarios can be simulated.

901 This simulation method was able to examine the error sources and influence factors affecting

902 flux error in more detail. Also important is that the [NOx]/[NO$_2$] ratio correction effect of flux

903 measurement was clarified.

904

905 *Data availability*. The data used in this analysis are available from the authors upon re-

906 quest.

907 *Author contributions*. Ang Li, Thomas Wagner and Yeyuan Huang developed the simula-

908 tion method. Yeyuan Huang, Yang Wang and Zhaokun Hu designed the forward model.

909 Hongmei Ren and Bing Dang processed the wind data. Julia Remmers performed the AMF

910 simulation. Pinhua Xie, Thomas Wagner, Jin Xu and Xiaoyi Fang supervised this study.

911 Yeyuan Huang analyzed the data and wrote the paper. Yang Wang revised this paper prelimi-

912 narily.

913 *Competing interests*. The authors declare that they have no competing interests.

914 *Acknowledgements.* This work was supported by National Natural Science Foundation of

915 China (grant nos. 41775029, 91644110 and 41530644), National Key Research and Devel-

916 opment Project of China 2018YFC0213201and 2017YFC0209902, Science and Technology

917 Commission Shanghai Municipality Research Project 17DZ1203102.

918

919 **References**

920 Alicke, B., Platt, U., Stutz, J.: Impact of nitrous acid photolysis on the total hydroxyl radical

921     budget during the Limitation of Oxidant Production/Pianura Padana Produzione di Ozono

922     study in Milan, J. Geophys. Res., 107, NO. D22, 8196, doi:10.1029/2000JD000075, 2002.

923 Arystanbekova, N.Kh.: Application of Gaussian plume models for air pollution simulation at

924     instantaneous emissions. Mathematics and Computers in Simulation, 67, 4-5.

925     https://doi.org/10.1016/j.matcom.2004.06.023, 2004.

926 Bobrowski, N., Honninger, G., Galle, B., and Platt U.: Detection of bromine monoxide in a

927     volcanic plume, Nature, 423, 273–276,2003.

928 Beirle, S., Hörmann, C., Penning de Vries, M., Dörner, S., Kern, C., and Wagner, T.: Estimat-

929 ing the volcanic emission rate and atmospheric lifetime of $SO_2$ from space: a case study for

930 Kīlauea volcano, Hawai`i, Atmos. Chem. Phys., 14, 8309–8322,

931 https://doi.org/10.5194/acp-14-8309-2014, 2014.

932 Beirle, S., Platt, U., Wenig, M., and Wagner, T.: Weekly cycle of $NO_2$ by GOME measure-

933 ments: a signature of anthropogenic sources, Atmos. Chem. Phys., 3, 2225–2232,

934 https://doi.org/10.5194/acp-3-2225-2003, 2003.

935 Berg, N., Mellqvist, J., Jalkanen, J.-P., and Balzani, J.: Ship emissions of $SO_2$ and $NO_2$:

936 DOAS measurements from airborne platforms, Atmos. Meas. Tech., 5, 1085–1098,

937 https://doi.org/10.5194/amt-5-1085-2012, 2012.

938 Danckaert, T., Fayt, C., van Roozendael, M., de Smedt, I., Letocart, V., Merlaud, A., and Pi-

939 nardi, G.: QDOAS Software user manual, available at:

940 http://uv-vis.aeronomie.be/software/QDOAS/QDOAS_manual.pdf (last access: 9 Septem-

941 ber 2016), 2015.

942 Davis, Z. Y. W., Baray, S., McLinden, C. A., Khanbabakhani, A., Fujs, W., Csukat, C., Debosz,

943 J. and McLaren, R.: Estimation of NOx and $SO_2$ emissions from Sarnia, Ontario, using a

944 mobile MAX-DOAS (Multi-AXis Differential Optical Absorption Spectroscopy) and a

945 NOx analyzer, Atmos. Chem. Phys., 19, 13871–13889,

946 https://doi.org/10.5194/acp-19-13871-2019, 2019.

947 de Visscher, Alex.: AIR DISPERSION MODELING Foundations and Applications, ISBN

948 978-1-118-07859-4, Wiley, New York, 2014.

949 Deutschmann, T.; Beirle, S.; Frieß, U.; Grzegorski, M.; Kern, C.,Kritten, L.; Platt, U.; Pra-

950 dos-Roman, C.; Pukite, J.; Wagner, T.; Werner, B.; Pfeilsticker, K., The Monte Carlo at-

951 mospheric radiative transfer model McArtim: introduction and validation of Jacobians and

952 3-D features, J. Quant. Spectrosc. Ra., 112, 1119–1137, 2011,

953 https://doi.org/10.1016/j.jqsrt.2010.12.009.

954 Ding, J., van der A, R. J., Mijling, B., Levelt, P. F., and Hao, N.: NOx emission estimates dur-

955 ing the 2014 Youth Olympic Games in Nanjing, Atmos. Chem. Phys., 15, 9399–9412,

956 https://doi.org/10.5194/acp-15-9399-2015, 2015.

957 Deutschmann, T.; Beirle, S.; Frieß, U.; Grzegorski, M.; Kern, C.,Kritten, L.; Platt, U.; Pra-

958 dos-Roman, C.; Pukite, J.; Wagner, T.; Werner, B.; Pfeilsticker, K., The Monte Carlo at-

959 mospheric radiative transfer model McArtim: introduction and validation of Jacobians and

960 3-D features, J. Quant. Spectrosc. Ra., 2011, 112, 1119–1137.

961 Edmonds, M., Herd, R. A., Galle, B., and Oppenheimer, C. M.: Automated high-time resolu-

962 tion measurements of $SO_2$ flux at Soufrière Hills Volcano, Montserrat, B. Volcanol., 65,

963 578–586, 2003.

964 Frins, E., Bobrowski, N., Osorio, M., Casaballe, N., Belsterli, G., Wagner, T. and Platt, U.:

965 Scanning and mobile Multi-Axis DOAS measurements of $SO_2$ and $NO_2$ emissions from an

966 electric power plant in Montevideo, Uruguay. Atmos. Environ., 98, 347–356.

967 https://doi.org/10.1016/j.atmosenv.2014.03.069, 2014.

968 Galle, B., Oppenheimer, C., Geyer, A., McGonigle, A.J.S., Edmonds, M. and Horrocks, L.: A

969 miniaturized ultraviolet spectrometer for remote sensing of $SO_2$ fluxes: A new tool for vol-

970 cano surveillance. J. Volcanol. Geother. Res., 119, 241–254, 2003.

971 Hönninger, G., von Friedeburg, C., and Platt, U.: Multi axis differential optical absorption

972 spectroscopy (MAX-DOAS), Atmos. Chem. Phys., 4, 231–254,

973 https://doi.org/10.5194/acp-4-231-2004, 2004.

974 Ibrahim, O., Shaiganfar, R., Sinreich, R., Stein, T., Platt, U., and Wagner, T.: Car

975 MAX-DOAS measurements around entire cities: quantification of NOx emissions from the

976 cities of Mannheim and Ludwigshafen (Germany), Atmos. Meas. Tech., 3, 709–721,

977 https://doi.org/10.5194/amt-3-709-2010, 2010.

978 Jin, J., Ma, J., Lin, W., Zhao, H., Shaiganfar, R., Beirle, S., and Wagner, T.: MAX-DOAS

979 measurements and satellite validation of tropospheric $NO_2$ and $SO_2$ vertical column densi-

980 ties at a rural site of North China, Atmos. Environ., 133, 12–25,

981 https://doi.org/10.1016/j.atmosenv.2016.03.031, 2016.

982 Johansson, M., Galle, B., Yu, T., Tang, L., Chen, D., Li, H., Li, J., Zhang, Y.: Quantification of

983 total emission of air pollutants from Beijing using mobile mini-DOAS. Atmos. Environ.,

984 42,6926–6933. https://doi.org/10.1016/j.atmosenv.2008.05.025, 2008.

985    Johansson, M., Rivera, C., de Foy, B., Lei, W., Song, J., Zhang, Y., Galle, B., and Molina, L.:

986       Mobile mini-DOAS measurement of the outflow of $NO_2$ and HCHO from Mexico City,

987       Atmos. Chem. Phys., 9, 5647–5653, https://doi.org/10.5194/acp-9-5647-2009, 2009.

988    Kraus, S.: DOASIS, A Framework Design for DOAS, PhD thesis, University of Mannheim

989       (http://hci.iwr.uni-heidelberg.de/publications/dip/2006/Kraus PhD2006.pdf), 2006.

990    Lushi, E., Stockie, J. M.: An inverse Gaussian plume approach for estimating atmospheric

991       pollutant emissions from multiple point sources. Atmos. Environ., 44, 1097-1107.

992       https://doi.org/10.1016/j.atmosenv.2009.11.039, 2009.

993    Merlaud, A., Tack, F., Constantin, D., Georgescu, L., Maes, J., Fayt, C., Mingireanu, F.,

994       Schuettemeyer, D., Meier, A. C., Schönardt, A., Ruhtz, T., Bellegante, L., Nicolae, D., Den

995       Hoed, M., Allaart, M., and Van Roozendael, M.: The Small Whiskbroom Imager for at-

996       mospheric compositioN monitorinG (SWING) and its operations from an unmanned aerial

997       vehicle (UAV) during the AROMAT campaign, Atmos. Meas. Tech., 11, 551–567,

998       https://doi.org/10.5194/amt-11-551-2018, 2018.

999    Platt, U. and Stutz, J.: Differential Optical Absorption Spectroscopy (DOAS), Principles and

1000      Applications, ISBN 978-3-540-21193-8, Springer, Berlin-Heidelberg, 2008.

1001    Richter, A., Burrows, J. P., Nüß, H., Granier, C., and Niemeier, U.: Increase in tropospheric

1002      nitrogen dioxide over China observed from space, Nature, 437, 129–132, 2005.

1003    Rivera, C., Sosa, G., Wöhrnschimmel, H., de Foy, B., Johansson, M., and Galle, B.: Tula in-

1004      dustrial complex (Mexico) emissions of $SO_2$ and $NO_2$ during the MCMA 2006 field cam-

1005      paign using a mobile mini-DOAS system, Atmos. Chem. Phys., 9, 6351–6361,

1006      https://doi.org/10.5194/acp-9-6351-2009, 2009.

1007    Seinfeld, J. H. and Pandis, S. N.: Atmospheric Chemistry and Physics – From Air Pollution to

1008      Climate Change, John Wiley, New York, 1998.

1009    Shaiganfar, R., Beirle, S., Sharma, M., Chauhan, A., Singh, R. P., and Wagner, T.: Estimation

1010      of NOx emissions from Delhi using Car MAX-DOAS observations and comparison with

1011      OMI satellite data, Atmos. Chem. Phys., 11, 10871–10887,

1012      https://doi.org/10.5194/acp-11-10871-2011, 2011.

1013 Shaiganfar, R., Beirle, S., Denier van der Gon, H., Jonkers, S., Kuenen, J., Petetin, H., Zhang,

1014      Q., Beekmann, M., and Wagner, T.: Estimation of the Paris NOx emissions from mobile

1015      MAX-DOAS observations and CHIMERE model simulations during the MEGAPOLI

1016      campaign using the closed integral method, Atmos. Chem. Phys., 17, 7853–7890,

1017      https://doi.org/10.5194/acp-17-7853-2017, 2017.

1018 Spicer, C. W.: Nitrogen Oxide Reactions in the Urban Plume of Boston. Science, 215, 1095–

1019      1097. http://www.sciencemag.org/cgi/doi/10.1126/science.215.4536.1095, 1982.

1020 Theys, N., Van Roozendael, M., Hendrick, F., Fayt, C., Hermans, C., Baray, J. L., Goutail, F.,

1021      Pommereau, J. P., De Maziere, M.: Retrieval of stratospheric and tropospheric BrO col-

1022      umns from multi-axis DOAS measurements at Reunion Island (21 ° S, 56 ° E). Atmos.

1023      Chem. Phys., 18, 4733-4749, https://doi.org/10.5194/acp-7-4733-2007, 2007.

1024 Vandaele, A. C., Simon P. C., Guilmot, J. M. Carleer, M., Colin, R.: SO2 absorption cross

1025      section measurement in the UV using a Fourier transform spectrometer, J. Geophys. Res.,

1026      99, D12, https://doi.org/10.1029/94JD02187, 1994.

1027 Vandaele, A.C., Hermans, C., Simon, P.C., Carleer, M., Colin, R., Fally, S., Mérienne, M.F.,

1028      Jenouvrier, A., Coquart, B.: Measurements of the NO2 absorption cross-section from 42

1029      000 cm−1 to 10000 cm−1 (238–1000 nm) at 220 K and 294 K, J. Quanr. .Specrrosc. Radior.

1030      Transfer, 59,171-184, DOI: 10.1016/S0022-4073(97)00168-4, 1998.

1031 Wagner, T., Dix B., Friedeburg, C. v., Frieß, U., Sanghavi, S., Sinreich, R., and Platt, U.:

1032      MAX-DOAS $O_4$ measurements –a new technique to derive information on atmospheric

1033      aerosols -Principles and information content, J. Geophys. Res., 109, D22205,

1034      https://doi.org/10.1029/2004JD004904, 2004.

1035 Wagner, T., Ibrahim, O., Shaiganfar, R., and Platt, U.: Mobile MAX-DOAS observations of

1036      tropospheric trace gases, Atmos. Meas. Tech., 3, 129–140,

1037      https://doi.org/10.5194/amt-3-129-2010, 2010.

1038 Wagner, T., Beirle, S., Brauers, T., Deutschmann, T., Frieß, U., Hak, C., Halla, J. D., Heue, K.

1039      P., Junkermann, W., Li, X., Platt, U., and Pundt-Gruber, I.: Inversion of tropospheric pro-

1040      files of aerosol extinction and HCHO and $NO_2$ mixing ratios from MAX-DOAS observa-

1041    tions in Milano during the summer of 2003 and comparison with independent data sets,

1042    Atmos. Meas. Tech., 4, 2685–2715, https://doi.org/10.5194/amt-4-2685-2011, 2011.

1043    Walter, D., Heue, K. P., Rauthe‐Schöch, A., Brenninkmeijer, C. A. M., Lamsal,L. N., Krot-

1044    kov, N. A. Platt, U.: Flux calculation using CARIBIC DOAS aircraft measurements: SO$_2$

1045    emission of Norilsk, J. Geophys. Res., 117, D11305, https://doi.org/10.1029/2011JD017335,

1046    2012.

1047    Wang, T., Hendrick, F., Wang, P., Tang, G., Clémer, K., Yu,H., , Fayt C., Hermans, C., Gielen,

1048    C., Müller, J.-F., Pinardi, G.,Theys, N., Brenot, H., Roozendael, M. Van.: Evaluation of

1049    tropospheric SO2 retrieved from MAX-DOAS measurements in Xianghe, China,   Atmos.

1050    Chem. Phys., 14, 11149–11164, doi:10.5194/acp-14-11149-2014, 2014.

1051    Wu, F. C., Xie, P. H., Li, A., Chan, K. L., Hartl, A., Wang, Y., Si, F. Q., Zeng, Y., Qin, M., Xu,

1052    J., Liu, J. G., Liu, W. Q., and Wenig, M.: Observations of SO$_2$ and NO$_2$ by mobile DOAS in

1053    the Guangzhou eastern area during the Asian Games 2010, Atmos. Meas. Tech., 6, 2277–

1054    2292, https://doi.org/10.5194/amt-6-2277-2013, 2013.

1055    Wu, F., Xie, P., Li, A., Mou, F., Chen, H., Zhu, Y., Zhu, T., Liu, J., and Liu, W.: Investigations

1056    of temporal and spatial distribution of precursors SO$_2$ and NO$_2$ vertical columns in the

1057    North China Plain using mobile DOAS, Atmos. Chem. Phys., 18, 1535–1554,

1058    https://doi.org/10.5194/acp-18-1535-2018, 2018.

1059    Zhang, H.X., Liu, C., Hu Q.H., Cai, Z.N., Su W.J., Xia, C.Z., Zhu Y.Z., Wang, S.W., Liu J.G.:

1060    Satellite UV-Vis spectroscopy: implications for air quality trends and their driving forces in

1061    China    during    2005–2017.    Light    Sci.    Appl.,    8,    100    (2019),

1062    https://doi.org/10.1038/s41377-019-0210-6, 2019.

1063    Zhang, H.X., Liu, C., Chan, K.L., Hu, Q.H., Liu, H.R., Li, B., Xing, C.Z., Tan, W., Zhou, H.J.,

1064    Si, F.Q., Liu, J.G.: First observation of tropospheric nitrogen dioxide from the Environ-

1065    mental Trace Gases Monitoring Instrument onboard the GaoFen-5 satellite. Light Sci. Appl.,

1066    9, 66(2020), https://doi.org/10.1038/s41377-020-0306-z, 2020.

1067 **Appendix**

1068 **1. NOx simulation results (relative error)**
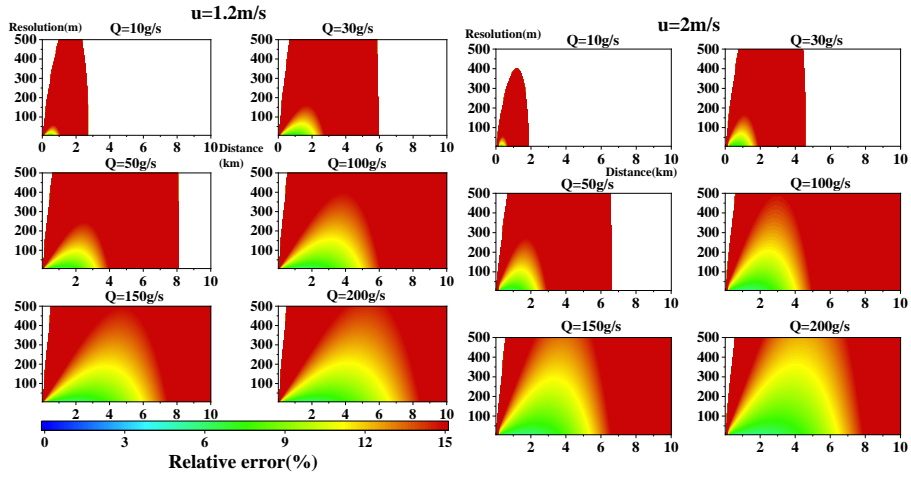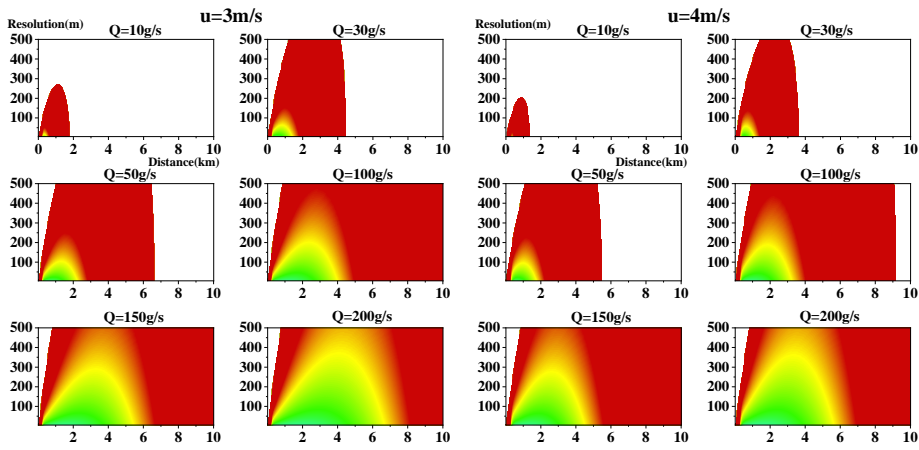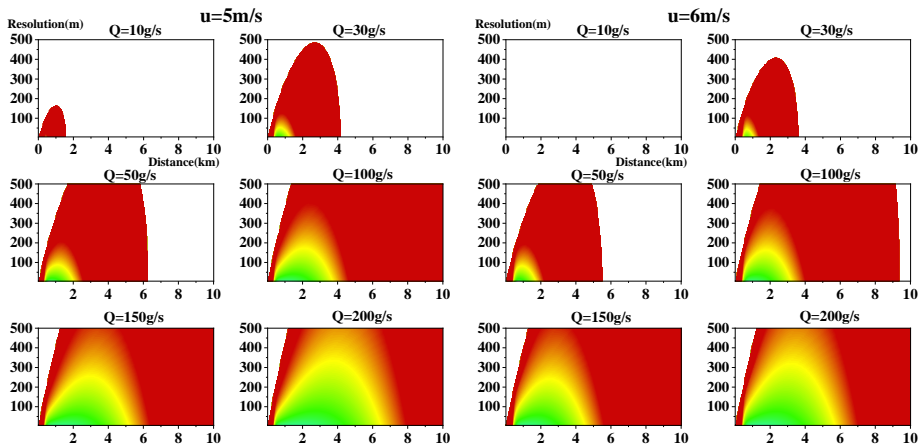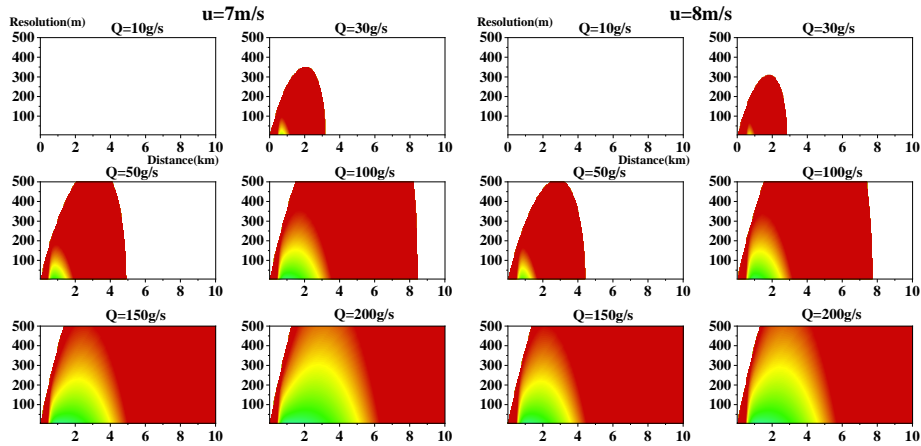
1072

1073 Figure 25. Relative errors (using Eq. 17) of NOx as a function of the measurement distance from the source

1074 (*x*-axis) and the sampling resolution (*y*-axis). The different subfigures show the results for different wind

1075 speeds and different emission rates. The color map indicates the relative errors.

1076 **2. SO$_2$ simulation results (relative error)**
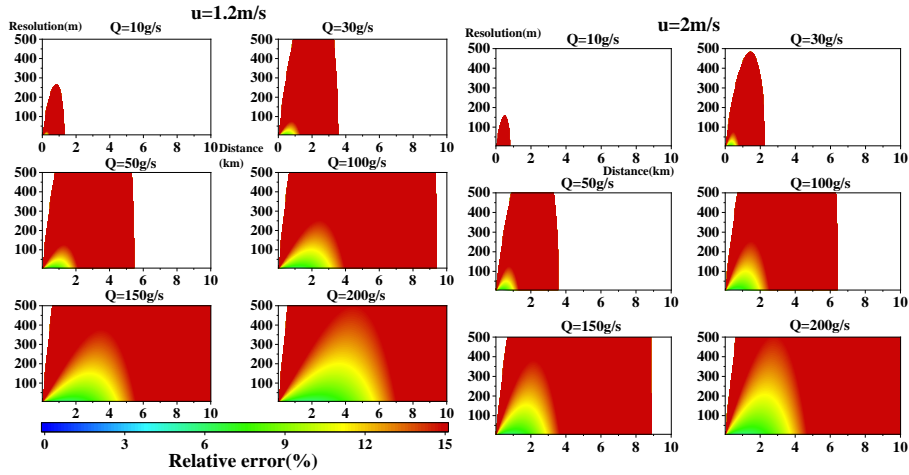
1077
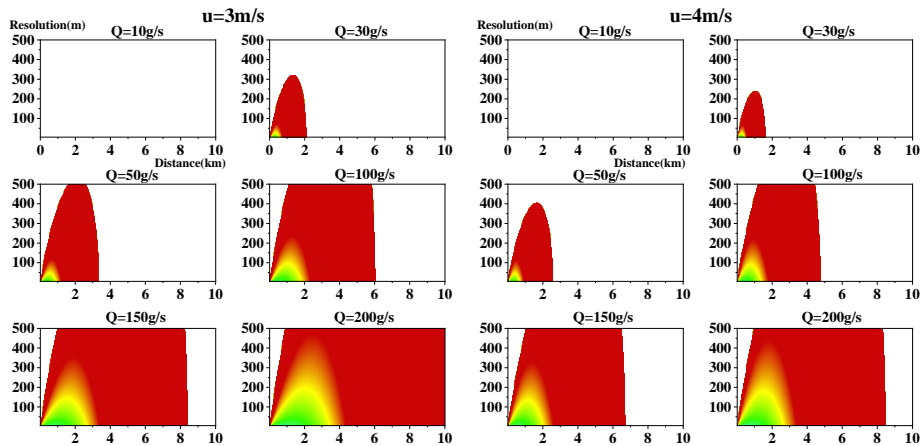
1078

1079
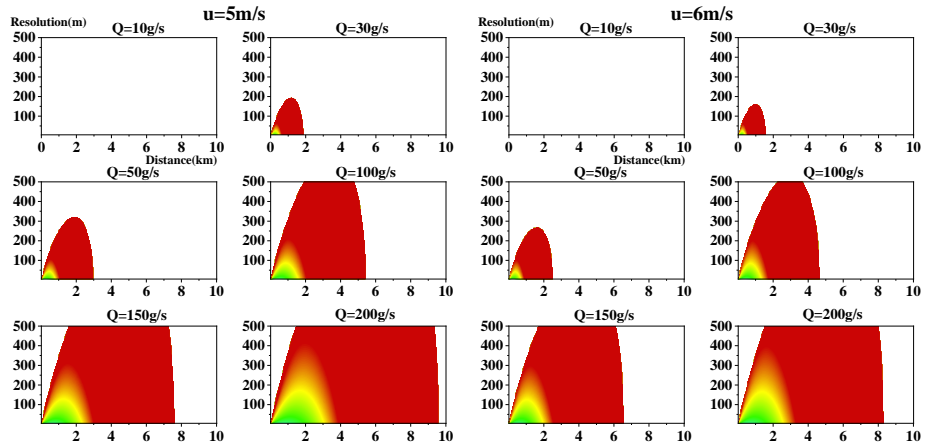
1080

1081 Figure 26. Relative error (using Eq. 16) of the distribution of $SO_2$ for different wind fields of different

1082 emission rates. The unit of all abscissas is the measurement distance from the source (km), while that

1083 of the ordinate is the sampling resolution (m). The color map indicates the relative errors.